

*Hubble Space Telescope Astrometry of the Procyon System*¹

Howard E. Bond,^{2,3} Ronald L. Gilliland,^{3,4} Gail H. Schaefer,⁵ Pierre Demarque,⁶
 Terrence M. Girard,⁶ Jay B. Holberg,⁷ Donald Gudehus,⁸ Brian D. Mason,⁹
 Vera Kozhurina-Platais,³ Matthew R. Burleigh,¹⁰ Martin A. Barstow,¹⁰ and
 Edmund P. Nelan³

Received _____; accepted _____

¹Based on observations with the NASA/ESA *Hubble Space Telescope* obtained at the Space Telescope Science Institute, and from the Mikulski Archive for Space Telescopes at STScI, which are operated by the Association of Universities for Research in Astronomy, Inc., under NASA contract NAS5-26555

²Department of Astronomy & Astrophysics, Pennsylvania State University, University Park, PA 16802, USA; heb11@psu.edu

³Space Telescope Science Institute, 3700 San Martin Dr., Baltimore, MD 21218, USA

⁴Center for Exoplanets and Habitable Worlds, Department of Astronomy & Astrophysics, Pennsylvania State University, University Park, PA 16802, USA

⁵The CHARA Array of Georgia State University, Mount Wilson Observatory, Mount Wilson, CA 91023, USA

⁶Department of Astronomy, Yale University, Box 208101, New Haven, CT 06520, USA

⁷Lunar & Planetary Laboratory, University of Arizona, 1541 E. University Blvd., Tucson, AZ 85721, USA

⁸Department of Physics & Astronomy, Georgia State University, Atlanta, GA 30303, USA

⁹U.S. Naval Observatory, 3450 Massachusetts Ave., Washington, DC 20392, USA

¹⁰Department of Physics & Astronomy, University of Leicester, Leicester LE1 7RH, UK

ABSTRACT

The nearby star Procyon is a visual binary containing the F5 IV-V subgiant Procyon A, orbited in a 40.84 yr period by the faint DQZ white dwarf Procyon B. Using images obtained over two decades with the *Hubble Space Telescope*, and historical measurements back to the 19th century, we have determined precise orbital elements. Combined with measurements of the parallax and the motion of the A component, these elements yield dynamical masses of $1.478 \pm 0.012 M_{\odot}$ and $0.592 \pm 0.006 M_{\odot}$ for A and B, respectively.

The mass of Procyon A agrees well with theoretical predictions based on asteroseismology and its temperature and luminosity. Use of a standard core-overshoot model agrees best for a surprisingly high amount of core overshoot. Under these modeling assumptions, Procyon A’s age is ~ 2.7 Gyr.

Procyon B’s location in the H-R diagram is in excellent agreement with theoretical cooling tracks for white dwarfs of its dynamical mass. Its position in the mass-radius plane is also consistent with theory, assuming a carbon-oxygen core and a helium-dominated atmosphere. Its progenitor’s mass was $1.9\text{--}2.2 M_{\odot}$, depending on its amount of core overshoot.

Several astrophysical puzzles remain. In the progenitor system, the stars at periastron were separated by only ~ 5 AU, which might have led to tidal interactions and even mass transfer; yet there is no direct evidence that these have occurred. Moreover the orbital eccentricity has remained high (~ 0.40). The mass of Procyon B is somewhat lower than anticipated from the initial-to-final-mass relation seen in open clusters. The presence of heavy elements in its atmosphere requires ongoing accretion, but the place of origin is uncertain.

Subject headings: astrometry — stars: binaries: visual — stars: fundamental

– 3 –

parameters — stars: individual (Procyon) — stars: white dwarfs

1. Introduction

An early triumph of positional astronomy was the discovery of astrometric perturbations of the motions of Procyon and Sirius by Bessel (1844), who attributed them to the gravitational influence of unseen companions. In 1862, Sirius B was seen by Alvan G. Clark,¹ verifying Bessel’s supposition. Procyon (α Canis Minoris) proved more recalcitrant: many visual observers attempted during the rest of the 19th century to detect its companion, but without success—even though by this time it was known from the astrometry that the orbital period is about 40 yr (Auwers 1873), and even approximately where the companion should be located. Struve (1874) reported an extremely faint companion of Procyon, but his claim was subsequently withdrawn and conceded to be spurious. Extensive attempts at the U.S. Naval Observatory (USNO) in 1874 and 1876 also failed (Davis 1876). Finally, more than five decades after Bessel’s announcement, the faint companion of Procyon was seen visually by Schaeberle (1896) at the Lick Observatory 36-inch refractor. The history of the 19th-century searches for Procyon B was colorfully summarized by See (1898)—who called the Procyon system “the most magnificent which astronomical observation has yet disclosed”—and later by Spencer Jones (1928).

The companion, Procyon B (WD 0736+053), with a visual magnitude of 10.82 (Provencal et al. 2002, hereafter P02), is 10.5 mag fainter than its primary, and is never separated by more than $\sim 5''$ from Procyon A. Visual detection of Procyon B is thus notoriously difficult. For example, Schaeberle (1897) remarked that it is “useless to look for either of these companions [of Procyon and Sirius] with the 36-inch telescope when the seeing is not good.” At the Yerkes Observatory, the eminent visual observer Barnard (1913) noted that “it requires the best conditions to even see it.” Charles Worley, double-star observer at the USNO, asserted to two of us, more than two decades ago, that he was the

¹Clark’s discovery was reported, and confirmed, by Bond (1862).

only living astronomer who had seen Procyon B with his own eye.

Nevertheless, visual measurements of the separation and position angle of Procyon B slowly accumulated over the first third of the 20th century, along with absolute astrometry and radial-velocity (RV) measurements of Procyon A. Comprehensive analyses of these data were made by Spencer Jones (1928) and Strand (1951, hereafter S51), yielding dynamical masses for the two components (M_A and M_B) of 1.24 and 0.39 M_\odot , and 1.74 and 0.63 M_\odot , respectively. Procyon A is a slightly evolved subgiant of spectral type F5 IV-V (e.g., Gray et al. 2001). The very low luminosity of B relative to its mass indicated that it must be a white dwarf (WD), as deduced by Kuiper (1937). In fact, it is the third brightest WD in the sky after Sirius B and α^2 Eridani B—but it was not possible to obtain its spectrum until the advent of the *Hubble Space Telescope* (*HST*). Using *HST* spectra, P02 showed that Procyon B has a spectral type of DQZ (i.e., a WD whose spectrum is devoid of hydrogen and shows features due to carbon, magnesium, and iron).

Irwin et al. (1992, hereafter I92) discussed precise RVs of Procyon A and re-analyzed the published astrometry. Their fit to these combined data yielded masses of 1.75 and 0.62 M_\odot , very close to the values reported by S51 four decades earlier. However, it had been pointed out by several authors (e.g., Hartmann, Garrison, & Katz 1975; Steffen 1985; Demarque & Guenther 1988; Guenther & Demarque 1993) that stellar models that match the observed luminosity and effective temperature of Procyon A require its mass to be close to 1.50 M_\odot . I92 noted that the discrepancy could be resolved if the semimajor axis of the relative orbit of B around A (at that time still based entirely on visual observations) were systematically too large by $\sim 0''.2$.

Girard et al. (2000, hereafter G00) measured some 600 photographic exposures, spanning 83 years, to redetermine the parallax and astrometric motion of Procyon A. To this analysis they added measurements of the A–B separation made in 1995 from a

ground-based near-infrared coronagraphic observation, and from an observation obtained with the Wide Field Planetary Camera 2 (WFPC2) on *HST*. This study resulted in a substantially reduced dynamical mass of $1.497 \pm 0.036 M_{\odot}$ for Procyon A, along with $0.602 \pm 0.015 M_{\odot}$ for the WD. The discrepancy with stellar theory thus appeared to have been removed. (It proved to be correct, as anticipated by I92, that the visual determination of the relative semi-major axis had been too large by about $0''.2$ —although this conclusion was still based almost entirely on the single *HST* observation.)

However, the mass of Procyon A remained a subject of debate over the years following the G00 publication, with several investigators, both theoretical and observational, advocating even lower values. Allende Prieto et al. (2002), adopting a smaller parallax and giving higher weight to the 1995 WFPC2 separation measurement, found a mass of $1.42 \pm 0.06 M_{\odot}$. Kervella et al. (2004), on the basis of asteroseismic data and an interferometric measurement of the angular diameter of Procyon A, argued that its mass is as low as $\sim 1.4 M_{\odot}$. Relatively low masses for both components were also deduced by Gatewood & Han (2006), who found 1.431 ± 0.034 and $0.578 \pm 0.014 M_{\odot}$ in an analysis that included their astrometric data on Procyon A from the Allegheny Observatory Multichannel Astrometric Photometer (MAP). But Guenther et al. (2008) emphasized again that masses this low are difficult to reconcile with stellar models, which require a mass close to $1.5 M_{\odot}$. Recent discussions of these issues, and further references, are given by Chiavassa et al. (2012) and Liebert et al. (2013, hereafter L13).

As we have recounted, visual measurements of the orbit of Procyon B are subject to large systematic errors; and the pair is likewise difficult even for modern ground-based instrumentation. But in sharp contrast to ground-based observations, the Procyon system is easily resolved and measured in appropriately exposed *HST* images. Because of the importance of Procyon A as a fundamental calibrator of stellar physics on or near the main

sequence, and of the mass of Procyon B for our understanding of WDs, our team began a program of regular *HST* imaging of the system. Our aims were to obtain dynamical masses of both stars with the highest possible precision, and an accuracy limited only by factors such as the absolute parallax of the system. Moreover, precise relative astrometry of the binary can place limits on the presence of third bodies in the system, down to planetary masses. Our project began with WFPC2 in 1997 November, and we observed the Procyon system at a total of 11 epochs through 2007 October. We then continued the program with the Wide Field Camera 3 (WFC3), following its installation in place of WFPC2 during the 2009 Servicing Mission. Our WFC3 images were obtained at five epochs between 2010 February and 2014 September. In addition, the *HST* archive contains the 1995 observations mentioned above, and two more observations in 1997, for a grand total of 19 epochs between 1995 and 2014, covering almost half of the orbital period.

In this paper, we present the precise relative astrometry of the binary that results from the *HST* observations, determine the elements of the visual orbit, and derive updated dynamical masses for both stars. We then discuss the astrophysical implications for the two components, and place limits on the presence of third bodies in the system.

2. *HST* Observations

Procyon A, at $V = 0.34$ (Johnson & Morgan 1953), is the eighth brightest star in the sky. The companion WD is fainter at visual wavelengths by nearly a factor of 16,000. Astrometry of this binary, even with *HST*, therefore presents an observational challenge. It is too bright for astrometric observations with the Fine Guidance Sensors (FGS). With WFPC2, whose shortest allowable exposure time was 0.11 s, it was possible to obtain unsaturated images of Procyon A only by using a filter bandpass, F218W, located at the short-wavelength extreme of the CCD detector sensitivity. The approach we adopted was

therefore to take a short, unsaturated exposure on Procyon A, and then, without moving the telescope, a second exposure long enough to detect Procyon B with good signal-to-noise ratio (SNR). This procedure was then repeated at several additional dithered positions (typically for a total of five exposure pairs) during the *HST* orbit. All of our WFPC2 observations were taken with the F218W ultraviolet filter, as were the 1995 archival frames mentioned above. A further advantage of observing in the ultraviolet is that the contrast between the stars is reduced to a factor of about 2,600, due to the WD being somewhat hotter than Procyon A. In addition to these frames, the archive contains images taken at two epochs in 1997, using the F1042M filter at the long-wavelength end of the WFPC2 sensitivity.² Procyon A is saturated in these frames. For all of the WFPC2 observations, Procyon was placed near the center of the Planetary Camera (PC) CCD, which has a plate scale of $0''.0454 \text{ pixel}^{-1}$. We requested telescope roll angles such that Procyon B would not lie near the diffraction spikes or charge bleeding of the bright component.

When the much more sensitive WFC3 was installed in place of WFPC2, it became impossible to obtain unsaturated images of Procyon A in any of the available filters, even using the shortest allowable exposure time of 0.5 s. Our approach was instead to take fairly deep dithered images, yielding a good SNR on Procyon B, and to locate the centroid of Procyon A using features (primarily the diffraction spikes) outside the saturated center of its image. For the WFC3 images, we chose the UVIS channel (plate scale $0''.0396 \text{ pixel}^{-1}$) and its near-infrared narrow-band F953N filter. Apart from the low system throughput in this filter—desirable for this particular application—an advantage of the long wavelength was the resolution of the diffraction spikes into a triple structure (due to the first Airy ring),

²There are also limited archival observations of Procyon obtained with WF/PC-1, NICMOS, and STIS, and with other WFPC2 filters than the ones we used, but we judged these unlikely to contribute additional useful astrometric data.

whereas these features are blended into a single blurred spike at shorter wavelengths. (On the other hand, the contrast between the stars in this filter is nearly a factor of 20,000.) For the WFC3 imaging, Procyon was placed near the center of a 512×512 subarray (in order to reduce data volume and improve observing efficiency).

Observing logs for the WFPC2 and WFC3 data are presented in Tables 1 and 2.

3. *HST* Astrometric Analyses

For the measurements of separation and position angle for the Procyon system, we have three distinct sets of *HST* data, each requiring different astrometric analysis techniques. These are (1) the (mostly) unsaturated images obtained with WFPC2 and the F218W filter; (2) a set of WFPC2 frames in the F1042M filter, in which Procyon A is saturated; and (3) the WFC3 images in F953N, in which Procyon A is also saturated.

3.1. WFPC2 Images in F218W

Figure 1 illustrates a typical pairing of a short unsaturated exposure in F218W for astrometry of Procyon A, and a much longer exposure at the same pointing used to analyze Procyon B. The inset in the center shows Procyon A from a 0.11-s exposure, superposed on a 100-s frame in which the WD is easily detected in spite of the neighboring, grossly overexposed image of the primary star.

In our first visit in 1997, we were too aggressive in choosing an exposure time for A of 0.14 s, resulting in its image containing saturated pixels in most of the exposures. Fortunately, due to dithering, there were two short-exposure frames in which A remained unsaturated. Even at the reduced 0.12 s used in the 1998 visit, two of the short exposures

were again saturated for Procyon A. For the remainder of the WFPC2 observations, we set the short exposures to the WFPC2 minimum of 0.11 s, and none of them were saturated.

In all cases we used the individual `c0m.fits` images from the archive pipeline for the astrometric analysis. These frames have bias subtraction and flat-fielding applied, but do not include any cosmic-ray removal, geometric correction, or drizzle processing. Each short- and long-exposure pair was taken at a different dither position, using fractional-pixel offsets to sample the point-spread function (PSF), plus shifts of a few integer pixels to average out the impact of detector defects (such as hot pixels). We checked for discrepant measurements due to cosmic-ray impacts, but found no cases where they had caused a problem in our relatively short integrations.

In the analysis of the 1995 WFPC2 observation by G00, the relative positions of Procyon A and B were determined by cross-correlation of the short-exposure image of A with the long-exposure image of B. The uncertainty for this measurement was at a level of about ± 0.2 pixels ($\sim 0''.009$). However, the accumulation of WFPC2 data from several programs, including ours, which used F218W between 1994 and 2009, makes it possible to apply a more precise astrometric analysis based on PSF fitting. (We did try the original cross-correlation approach for our WFPC2 data, but found that the errors were about 50% greater than those based on PSF fitting.)

PSF fitting is based on an empirically derived, over-sampled representation of the image structure, obtained by combining numerous high-SNR exposures taken at many independent pointings. As indicated in Table 1, we have 53 unsaturated exposures of 0.11 to 0.14 s on Procyon A. In addition, we included 96 archival observations of the standard star Grw +70°5824, obtained for WFPC2 F218W photometric calibrations between 1994 and 2009, and two frames of the standard star BD +17°4708 from 2004. That made a total of 151 well-exposed F218W images of stars having colors similar to Procyon A and B,

positioned near the center of the PC chip, for input to the PSF determination.

The approach we used is described in eqs. (2) and (3) of Gilliland et al. (1999). A uniform spatial grid on a scale finer than the native pixel size is first defined. (In this case, we chose a factor of 50 finer than the input scale, because it allowed re-use of existing codes developed for *Kepler* analyses, but the results are insensitive to the exact choice.)

The individual pixel values, after normalization of all inputs to unit volume, are accumulated into a weighted sum at each over-sampled grid point, using a Gaussian weighting based on separations of each input pixel from the accumulation grid. The width of the Gaussian weighting function is a free parameter. Adoption of too small a Gaussian width results in over-fitting the data, while too wide a weighting function suppresses available resolution in the resulting PSF. We used a Gaussian weighting width of 0.416 pixels full width half maximum (FWHM), which minimized the scatter in measurements at the same epoch.

Developing the over-sampled PSF requires precise knowledge of the relative centering of each input image. The solution is therefore iterative, since precise relative positions are best determined through fitting the over-sampled PSF to individual images. Fortunately a simple first-moment estimate of image positions for all inputs is accurate enough to start a rapidly convergent iterative cycle of determining an over-sampled PSF, revising the image positions, and recalculating the PSF.

With the PSF defined, we then obtained the relative positions of individual images of Procyon A and B by fitting a bi-cubic interpolation function (Press et al. 1992) to the PSF, and then employed a non-linear least-squares fit (Bevington 1969) to determine the relative x, y centers of both stars. These fits used the central 21 pixels (5×5 box without corners), after experiments showed that smaller or larger fit domains performed marginally less well.

Procyon B lies in the extended wings of the PSF of Procyon A. Simulations indicated that these wings shift the measured position of B by less than $0''.001$ at times of greatest separation early in the WFPC2 series, increasing to $0''.003$ – $0''.004$ near closest approach. We therefore derived a deep PSF by stacking all of the strongly saturated Procyon A images, which we then subtracted before performing PSF fits for the position of B.

WFPC2 had significant geometric distortion, due both to the camera optics and a manufacturing defect in the CCDs. We applied geometric-correction terms for the optical distortions, and the “34th-row” detector defect, from Gonzaga & Biretta (2010). The geometrically corrected x, y positions were then converted to angular units using a F218W plate scale of $0''.045437 \text{ pixel}^{-1}$, with a nominal fractional error of ± 0.0003 , adjusted slightly for differential velocity aberration (using the `VAFCTOR` keyword in the image headers), all as described by Gonzaga & Biretta.³

Because of our technique of short exposures followed by long exposures, our measurements of the separation and position angle are subject to a systematic offset due to telescope pointing drift (which occurs even when the telescope is locked on guide stars). Gilliland (2005) showed that drifts of $0''.010$ – $0''.015$ are typical during *HST* orbits, which translates to about $0''.0025$ for a pair of A, B exposures taken over about 1/5th of an *HST* visibility period.

³The WFPC2 CCDs also suffered from charge-transfer inefficiency (CTI), which increased with time over the years spent in the space environment. At low light levels, CTI can cause systematic shifts in the centroid locations of stellar images. However, in the case of our Procyon observations, involving bright stars and strong background light, the CTI effects on the astrometry are very small (e.g., Goudfrooij et al. 2006), and we did not make any corrections for them.

Since our images only show the two components of Procyon, we are unable to establish firmly that the pointing drift was always present, and if so what its direction was; but the effect of such drifts is likely to dominate over other terms (such as influence of differing stellar colors or changing telescope focus on the PSF, plate-scale changes due to telescope “breathing,” residual contamination from component A, etc.). We have therefore estimated the errors of the average positions at each epoch by combining in quadrature the standard error based on the observed measurement scatter with a systematic term of $\pm 0''.0025$ for telescope drift. (Although drift is systematic within a single *HST* visit, a range of different telescope orientations was used across the different epochs, so it is appropriate to treat drift error as a random term.)

Lastly, we determined the absolute J2000 position angle of B relative to A, using the ORIENTAT keyword in the image headers, which gives the orientation on the sky of the image y axis. The error on position angle includes two terms. The first arises from the errors of derived x, y positions of A and B, estimated as described above. This term in position angle will be inversely proportional to the lever arm provided by the changing separation of A and B during their orbit. A second term arises from uncertainties in the absolute *HST* roll angle. We assume a $1''$ error on guide-star positions, observed with the FGS over a $\sim 1000''$ baseline, which translates to an angular error of $\pm 0''.028$. We combine these two uncertainties in quadrature. The final astrometric results from the WFPC2 F218W images are given in Table 3, lines 1 and 4 through 14.

3.2. WFPC2 Images in F1042M

The *HST* archive contains images of Procyon in the WFPC2 F1042M filter obtained at two epochs in 1997. The primary aim of these observations was a search for faint companions of 23 nearby stars, including Procyon, but no new companions were found

by the proposing team (Schroeder et al. 2000). For our astrometric measurements, these frames raised the challenge that Procyon B is nicely exposed, but the core of the image of A is strongly saturated. This forced us to develop a means of using the outer portions of the PSF of Procyon A, where the spatial information is dominated by the diffraction spikes, to obtain its centroid location.

We faced a similar problem in our complementary *HST* program on the Sirius system, to be discussed in a separate forthcoming paper. Our WFPC2 images of Sirius were taken in the same F1042M filter, and are likewise saturated for Sirius A. In order to test methods for centroiding saturated images, we carried out a calibration program (Program ID: CAL/WFPC2-11509) on the star 109 Virginis (spectral type A0 V, $V = 3.73$). This star has a color similar to that of Sirius, and not extremely different from Procyon. It is sufficiently faint that unsaturated images in F1042M can be obtained in short exposures (0.23 s), along with saturated images from longer integrations (600 s). We obtained a set of three dithered pairs of short and long exposures on this star.⁴

We initially considered an approach for astrometric analysis of the saturated images of Procyon in which we would develop an over-sampled PSF for the unsaturated regions of the images, including especially the diffraction spikes. As in the case of the unsaturated F218W

⁴Janson et al. (2011) reported ground-based detection in the near-IR ($1.58\ \mu\text{m}$) of a companion to 109 Vir, at a separation of $0''.57$ and 6.04 mag fainter, epoch 2010.52. This object was also detected on 2009.27 and 2010.32 by L. C. Roberts et al. (private communication), at a similar position, and 5.4 mag fainter at $2.1\ \mu\text{m}$. They did not detect it at $1.25\ \mu\text{m}$. This location lies within the saturated pixels of our long *HST* exposures. In our short exposures at $1.04\ \mu\text{m}$ no companion is seen at the positions given by Janson et al. and Roberts et al. (nor anywhere else in the field), even though a 6-mag-fainter star would be readily detectable. This suggests that the companion is extremely red.

images described above, development of the PSF for saturated F1042M images requires an ensemble of input data. Table 4 lists the images of Sirius and 109 Vir that we used (in addition to the two sets of Procyon A F1042M images listed in Table 1).

However, we found that the appearance of the diffraction spikes is unstable. Figure 2 shows examples of the variable spike structures in saturated images of Sirius and Procyon in the F1042M filter. The intensities of the spikes vary by large amounts as functions of distance from the center of the stellar image in a quasi-periodic fashion, which does not reproduce well from epoch to epoch. The structure of these intensity variations appears to depend strongly on small differences in the location of the star in the field of view. Therefore we did not see any straightforward means of defining an over-sampled PSF for the unsaturated outer regions of the deep exposures.

We instead adopted an alternative approach of fitting straight lines to the diffraction spikes, and determining the image centroid from their intersection point. Our procedure was to estimate the location of the pixel nearest the center of the saturated image, and then search inwards toward this point along each of the four diffraction spikes until the first saturated pixel was encountered. From that pixel outward, we calculated the sums of intensities along each diffraction-spike axis and along the two neighboring parallel axes one pixel away on either side. These sums were accumulated in two sequential segments, each 30 pixels long, for a total length of 60 pixels. Then a parabola was fit to the three sums; the peak of this parabola marked the location of the diffraction-spike axis in the direction orthogonal to the spike. We found good consistency between results from the first and second 30-pixel segments along the spikes, and thus combined them to form a single center for each of the four spikes. The intersection point of the lines connecting the symmetric diffraction-spike centers then defined the stellar centroid.

Application of this approach to the three pairs of calibration frames on 109 Vir

gave mean offsets between the spike intersection point and the PSF-derived centroid of -0.004 ± 0.002 pixels in x , and $+0.044 \pm 0.040$ pixels in y (or, in arcseconds, $-0''.0002 \pm 0''.0001$ and $+0''.0020 \pm 0''.0018$, respectively; the errors are estimated from the scatter among the three measurements). We simply adopted these as (small) corrections to be added to the A-component positions from the long exposures.

To determine the centroids of Procyon B from the images, we followed the approach used for the F218W data. That is, an over-sampled PSF was first derived, using the same Gaussian weighting approach. We used 69 individual inputs, listed in Tables 1 and 4, consisting of all deep exposures of Procyon B and Sirius B in F1042M, plus the three unsaturated exposures on 109 Vir. Background removal was done by taking a median of an annulus from 13 to 23 pixels out from B, then subtracting it to remove the pedestal due to the wings of A.

Due to a MgF_2 lens immediately in front of the CCDs, there is a weak dependence of the WFPC2 plate scale on wavelength. A plate scale for F1042M images is not provided in Gonzaga & Biretta (2010). However, by plotting the plate scales listed by Gonzaga & Biretta against the index of refraction of MgF_2 at the effective wavelength of each filter, we found a tight, linear correlation. Only a slight extrapolation to the wavelength of F1042M was needed to estimate its plate scale. We adopted a relative plate scale of 1.00048 compared to the fiducial F555W value, for a net of $0''.045577 \text{ pixel}^{-1}$ for the PC chip.

Typical WFPC2 F1042M visits consisted of five or six exposures of about 8 s, and another five or six of about 60 s. Thus there are two distinct clumps of medium and long integrations. To see if there was a dependence of the astrometric results on exposure time, we compiled means and scatters within the medium and long blocks separately for each epoch. The average difference in measured separations from the medium- and long-exposure sets was an inconsequential $0''.0007$. The average scatter of separations was $0''.0026$ within

the medium exposures, and $0''.0035$ for the long exposures. We concluded that we could safely combine the results from all of the exposures within each epoch.

The remainder of the F1042M astrometric analysis proceeded as described above for the F218W images. However, the Procyon astrometry is not directly affected by *HST* pointing drift, since A and B are measured on the same frames. On the other hand, our results hinge on the single-orbit calibration using three pairs of short and long 109 Vir exposures, which *were* subject to the drift error. The canonical drift allowance of $0''.010$ – $0''.015$ per *HST* orbit visibility translates in this case into a potential systematic error of $\sim 0''.004$. We applied this value in quadrature with the the standard error based on random scatter. The astrometric results from the WFPC2 F1042M images are given in Table 3, lines 2 and 3.

3.3. WFC3 Images in F953N

The WFC3 observations of Procyon in F953N are similar to those in WFPC2 F1042M: Procyon A is saturated in all images. We adopted a similar approach for the analysis, beginning by assembling a set of images for PSF determination and a study of the use of diffraction spikes for centroiding. In addition to the WFC3 F953N images of Procyon, listed in Table 2, we have observed Sirius in this WFC3 filter in our complementary program on that binary. And we likewise carried out calibration observations (Program ID: GO-12598), in which we obtained both saturated and unsaturated WFC3 frames in F953N of the Pleiades main-sequence star HD 23886 (spectral type A3 V, $V = 8.01$). Table 5 lists the images of Sirius and HD 23886 that we used for these studies.

The data for all three targets were acquired using four-point dithering with the WFC3–UVIS–DITHER–BOX pattern. In most cases repeats were used at each setting within the pattern, providing 32 total exposures during each *HST* visit for Procyon, 28 for Sirius,

and 8 for HD 23886.

The HD 23886 calibration observations, and most of our Procyon observations, used Chip 2 of the WFC3 camera, with `UVIS2-C512C-SUB`, the 512×512 -pixel subarray nearest the Amp C readout. This subarray has been shown (Gilliland et al. 2010) to be the best behaved for photometry near and beyond saturation. The Sirius observations all used the larger `UVIS2-C1K1C-SUB` 1024×1024 subarray, also in Chip 2. However, our first WFC3 visit for Procyon in 2010 was obtained using the corresponding Chip 1 subarray. Lacking any supporting calibration observations for this chip, we have omitted the 2010 data from our analysis.

For the WFC3 astrometric analysis, we use the default drizzle-combined `drz.fits` images from the archive pipeline. These frames are created by combining the individual dithered exposures, and are fully processed to bias-subtracted, flat-fielded, and geometrically corrected images with cosmic rays removed.

The two left-hand panels in Figure 3 show two representative images of Procyon from our WFC3 F953N observations. In contrast to the WFPC2 frames in F1042M, the diffraction spikes have a smooth fall-off in intensity with radius, without any quasi-periodic fluctuations. Moreover, the image structure appears to be consistent over all of the epochs.

We therefore developed a deep PSF, using all of the F953N exposures in Tables 2 and 5, except for the short unsaturated exposure on HD 23886. This PSF extends out to a large enough radius always to cover the location of Procyon B; a small region around B was set to zero weight in each individual exposure contributing to the deep PSF. For the weighting we adopted a Gaussian weighting FWHM of 0.832 pixels. With the deep PSF determined, we then subtracted it before using data on B (both for development of the unsaturated, core PSF, and for the subsequent centroiding of B).

The two right-hand panels in Figure 3 show the result of subtracting the best-fit deep PSF from two individual images. A region around the primary-star charge bleeds is not handled well, but this is inconsequential. Apart from this, within the diffraction spikes, and generally for fine structures in the PSF from A, the subtraction effectively removes 85–90% of the flux.

As shown by the red boxes in Figure 3, we used only relatively small regions containing high-SNR but unsaturated point-like structures, in each of the four diffraction spikes, for the PSF fitting. The signal within these boxes exceeds that from B by over an order of magnitude.

Positions of B in all cases were determined using the PSF-fitting approach adopted for F218W. To create the PSF for this purpose, we started by stacking the 25 drizzled images of Procyon B, Sirius B, and HD 23886 (unsaturated). For the Procyon B and Sirius B inputs, the underlying light from A was first subtracted, using the deep over-sampled PSF of A.

Since we used two independent methods for fitting A and B in the same frames, and the PSFs do not have absolute centroids, it is important to apply a calibration using the images of HD 23886. We found that corrections of +0.468 pixels in x , and +0.449 pixels in y , needed to be added to the A-centroid technique results to bring them into alignment with the B technique. This leaves the possibility of telescope drift during the calibration observations unaccounted for. Fortunately, however, inspection of the HD 23886 images showed that it has a (previously unknown) faint companion, offset by ~ 20 pixels in x , and ~ 5 in y , from the bright star, which is detected in both the short and long exposures.⁵

⁵The companion of HD 23886 that we detected at epoch 2012.1290 is at separation $0''.804 \pm 0''.005$ and J2000 P.A. $228^\circ 94 \pm 0^\circ 35$, and is 5.6 mag fainter in F953N.

This allows a direct correction for *HST* pointing drift (particularly valuable in this case because one of the short/long pairs was split across two spacecraft orbits). Monitoring the faint-star position with unsaturated PSF fits in both the long and short exposures indicated a correction for drift of $+0.026$ and -0.018 pixels in x and y , respectively, in the above sense. Thus the net calibration zero-point corrections are $+0.494$ and $+0.431$ pixels in x and y . Since the companion is faint in the short exposures, the precision is rather low, and we adopt a systematic error term of $\pm 0''.004$ for the WFC3 astrometry within epochs. This was added in quadrature as a random term since visits are at effectively random orientations.

Although the pipeline images are geometrically corrected, at the time of our initial analyses the geometric distortion in F953N had not been calibrated as well as for the more frequently used WFC3 filters. In particular, it was not included in the study of WFC3 plate scales by Kozhurina-Platais (2014). However, a search of the *HST* archive yielded a set of frames in F953N of the cluster ω Centauri. We performed a new analysis of these images, generating new geometric-distortion calibration reference files paralleling those in the work just cited for other filters. After these files were incorporated into the calibration database at STScI, we retrieved the data again, and the results presented here make use of the new calibrations. The final plate scale adopted in the pipeline reductions for F953N is $0''.03962 \text{ pixel}^{-1}$. The results from this method are shown in Table 3 as the “WFC3 F953N PSF fit” entries.

Having developed the alternate technique of fitting straight lines to the diffraction spikes, and then taking the intersection of these lines as the centroid of component A for the F1042M data, we also applied this technique to the WFC3 F953N data. We again used the short and long exposures on HD 23886 to calibrate the offset between the spike-determined position of A and the PSF-determined position of B. In this case, the corrections are $+0.055$ and $+0.102$ pixels, to be applied to the position of A. The results from this method

are labelled in Table 3 as “WFC3 F953N spike fit” values. The largest absolute difference in A-B separation between the two methods over the four epochs is 5 mas, with a mean of 1.6 mas, and a standard deviation of 2.9 mas. This suggests that the two techniques yield comparable results, with differences between them consistent with the stated error bars. We therefore averaged the results, and show them at the bottom of Table 3, labelled “WFC3 F953N average.”

4. Orbital Solution

4.1. Compilation of Ground-based Measurements

Our *HST* measurements of the Procyon system are extremely precise, compared to ground-based data, but they cover less than half of only one orbital period. Thus the historical ground-based data are important in constraining the orbital elements, especially the period. The available visual observations of Procyon, from 1896 to 1932, were assembled by S51 (his Table 8). Since 1932, according to the Washington Double Star (WDS) Catalog maintained at the USNO, there have been only nine further published measurements of Procyon. Three of these measurements are from *HST* observations in 1995 and 1997 (G00; Schroeder et al. 2000), now superseded by our present results, and leaving only six new published ground-based observations since 1932.

The early observers would often report measurements averaged over several observations taken over relatively short intervals. Occasionally, the observer would recompute the averages in a subsequent publication based on a different combination of the measurements. This sometimes led to redundant listings for the same measurements. We cross-compared the S51 tabulation and WDS catalog with the original publications, and adopted the values published most recently by the observers. Additionally, in compiling his data, S51

sometimes averaged observations that had not been averaged by the original observers, and that are now listed individually in the WDS. In these instances, we adopted the individual measurements as listed in the WDS. Table 6 indicates the observations that we removed from the S51 and WDS listings, and which measurements we used to replace them.

Table 7 gives the complete list of edited ground-based measurements that were initially used in our orbit fit. Some of the observations were badly discrepant and were removed in our final fit; these are identified in the table by a superscript c in the first column. Our fitting procedure and rejection process are described below in §4.2. In his tabulation, S51 had corrected the position angles for precession to the J2000 equinox; in our Table 7 we have similarly corrected the position angles for the ground-based measurements after 1932 to the J2000 equinox (except for CCD and adaptive-optics observations, which we assumed to be reported for J2000).

4.2. Elements of the Relative Visual Orbit

We fitted a visual orbit simultaneously to the *HST* and ground-based measurements (Tables 3 and 7 respectively; for the *HST* WFC3 data, we used the “F953N average” values). We used a Newton-Raphson method to minimize χ^2 by calculating a first-order Taylor expansion for the equations of orbital motion. For the *HST* data we used the measurement errors directly from Table 3 in computing χ^2 . The ground-based observers typically did not estimate errors for their measurements, so we adopted an iterative approach to optimize the weighting of the ground-based data in our orbit fit, and to reject outliers. In the first step of the iterative procedure, we fit an orbit to the ground-based data only and applied uniform uncertainties to these measurements to force the reduced χ_ν^2 to equal unity (where ν is the degree of freedom). In the second step, we used these scaled uncertainties to fit an orbit simultaneously to the ground-based and *HST* measurements.

We used a sigma-clipping algorithm to reject any ground-based data point whose residual was more than three times the standard deviation of the residuals for the full data set. We repeated this procedure until no additional data points were rejected. The final data set contained the 57 measurements listed in Tables 3 and 7 (18 from *HST* and 39 ground-based retained in the solution). The adopted uncertainties for the ground-based separations were $\pm 0''.187$; we propagated this value to the position angle by assuming equal uncertainties in the right-ascension and declination directions. The historical measurements removed from the fit through sigma clipping are flagged in Table 7. Many of the rejected observations were made between 1914 and 1929, when the visual measurements were extremely difficult—or even, as suggested by S51, of doubtful reality.

Table 8 lists the final parameters for the visual orbit. The uncertainties were computed from the diagonal elements of the covariance matrix. We also investigated a solution using *only* the *HST* measurements; this solution produced uncertainties averaging about 60–70% larger than those presented in Table 8, with the error in the orbital period more than doubled. An additional, and probably final, *HST* observation will be scheduled in 2016, but we expect that the historical ground-based data will continue to be an essential part of the best orbital solution.

In Figure 4 we plot the data points, both *HST* and ground-based, and the orbital fit. The positions of Procyon B that are predicted from our orbital elements in Table 8 are marked with open blue circles, for the *HST* observations only. At the scale of Figure 4, the observed *HST* data (filled black circles) are so precise that they appear to lie exactly at the centers of the open blue circles. For a better visualization of the errors, the two panels of Figure 5 show the residuals of the *HST* observations from the positions predicted by our orbital elements, in right ascension and declination. The units are now milliarcseconds (mas), rather than the arcseconds of Figure 4. The error bars are those given in Table 3,

converted from separation and position angle to right ascension and declination. Based on the residual plots, there is no evidence within those errors for perturbations of the orbit by a third body. (We return to this point in §6.)

5. Determining Dynamical Masses

5.1. Parallax and Semimajor Axis of Procyon A

In addition to the elements of the relative orbit listed in Table 8, we need two further quantities in order to determine dynamical masses for both stars: the absolute parallax of the system, and the semimajor axis of the absolute motion of Procyon A on the sky.

There are three recent independent determinations of the parallax: (1) G00 obtained it from measurements of a series of ~ 50 plates taken at the USNO 1.55-m reflector between 1985 and 1990; (2) the parallax was measured by *Hipparcos* (we use the value from the new reduction by van Leeuwen 2007); and (3) it was measured with the Allegheny MAP by Gatewood & Han (2006). These results are in good agreement, and we adopt a weighted mean of the parallax values, as given in the top part of Table 9.

G00 determined the semimajor axis of Procyon A’s motion from ~ 600 exposures on plates obtained at six different observatories, from 1912 to 1995. We have adopted their result, $a_A = 1''.232 \pm 0''.008$, as given in the bottom of Table 9. It agrees fairly well with a value of $1''.217 \pm 0''.003$ obtained by S51 from a subset of the same photographic material.⁶ The G00 result differs by a larger amount from the $1''.179 \pm 0''.011$ found by I92 from a combined analysis of RVs and a re-analysis of S51’s astrometry.

⁶Strand actually gave a probable error of $\pm 0''.002$, which we have converted to standard error here.

Our decision to adopt the G00 value of a_A over that of S51—despite his quoted uncertainty being smaller—is based on the significant advantages of the G00 study. These include the use of plates spanning twice the time baseline (~ 80 yr vs. ~ 40 yr); digital centering with a laser-encoded PDS microdensitometer as opposed to visual centering with a single-screw measuring engine; and computer-calculated plate transformations using scores of reference stars compared to the four reference stars used in Strand’s manual calculations. It is possible that this last limitation of having to rely on just four reference stars might have caused Strand to underestimate the uncertainty in a_A . As a check on the uncertainty estimated by G00, Elliott Horch kindly reprocessed the 593 measures from G00 using his independent orbit-element code. The uncertainty in a_A was confirmed to be $\pm 0''.008$.

There is also the question of the sensitivity of the value of a_A derived by G00 to the adopted orbital elements, given our new and more precise determination of those elements. We investigated this by assuming the values in our Table 8 for all elements except the semimajor axis, and then reprocessing the photographic measures of G00, solving only for a_A . The result is unchanged and robust, with values of a_A ranging from $1''.231$ to $1''.234$, depending on the degree of “outlier” trimming. For these reasons, we have adopted the values of a_A and its uncertainty as given by G00.

5.2. Comparison with Radial Velocities

We did not use RV information in our orbital solution, which was based purely on astrometric data. The RVs, however, provide a useful check on the validity of our final results.

Our orbital elements, along with the parallax and the semimajor axis of Procyon A’s motion, allow us to predict the RV of Procyon A, apart from a constant offset due to the

center-of-mass motion of the binary system. In Figure 6 (top), we compare our predictions with absolute RVs published by I92 (from photographic spectrograms, 1909–1985), and a single absolute RV by Mosser et al. (2008, from RV speedometer). Also plotted are relative RVs by Innis et al. (1994; from RV spectrometer data, 1986–1990). Innis et al. adjusted their velocity zero-point so that their RVs would match the I92 orbit predictions in the mean. We have applied I92’s gamma-velocity of -4.115 km s^{-1} to our predicted RVs.

I92 also published a separate set of precise RVs of Procyon A, measured using a hydrogen-fluoride absorption cell, obtained over the interval 1980–1991. These velocities are on a relative scale. In Figure 6 (bottom), we compare the RVs predicted by our orbital elements with these velocities; we have arbitrarily shifted the zero-point of our predictions to match the measurements in the mean. Both of these figures show that our parameters of the Procyon system are able to predict the RV measurements very well.

5.3. Dynamical Masses

Table 10 lists the dynamical masses that result from our adopted parameters. We used the usual formulae for the total system mass, $M = M_A + M_B = a^3/(\pi^3 P^2)$, and for the individual masses, $M_A = M(1 - a_A/a)$ and $M_B = M a_A/a$; in these equations the masses are in M_\odot , a and π in arcseconds, and P in years.

In Table 11 we present the error budgets for the masses of Procyon A and B, based on the adopted random uncertainties of each of the parameters.⁷ For Procyon A, the

⁷A potential source of systematic uncertainty is errors in the plate scales of the *HST* cameras. Gonzaga & Biretta (2010) state a fractional uncertainty of ± 0.0003 for the WFPC2 plate scale, and for the WFC3 plate scale we derived a similar fractional uncertainty of ± 0.00018 . These imply a systematic uncertainty of about $0''.0013$ for the semimajor axis,

mass error is dominated almost entirely by the uncertainty in the parallax. For the WD companion, Procyon B, the parallax is again responsible for the majority of the error, but the uncertainty in the semimajor axis of Procyon A’s astrometric motion also contributes significantly. Unfortunately, the mass uncertainties are unlikely to be reduced in the near future, because Procyon is too bright for its parallax to be measured by the *Gaia* mission (D. Pourbaix, private communication).⁸

6. Limits on Third Body

As discussed in §4.2 and shown in the residuals plotted in Figure 5, we detected no significant perturbations in our orbital fit to the *HST* astrometry. These results allow us to place limits on the presence of third bodies orbiting either star in the Procyon system.

The stability of planets orbiting the individual stars in a binary system has been studied numerically by, among others, Holman & Wiegert (1999). Using the results in their Table 3, and the parameters of the present-day binary, we find that the longest periods for stable planetary orbits in the Procyon system are about 3.7 yr for a planet orbiting Procyon A, and 2.8 yr for one orbiting Procyon B.

We calculated the semimajor axes of the astrometric perturbations of both stars that would result from being orbited by planetary companions of masses ranging from 5 to $25 M_{\text{Jup}}$ (where M_{Jup} is the mass of Jupiter, $0.000955 M_{\odot}$), and for orbital periods up to the

a. Table 11 shows that a systematic error of this magnitude contributes negligibly to the random errors in the dynamical masses.

⁸*Gaia* may provide a slight improvement in the correction of ground-based parallaxes to absolute, by determining parallaxes for the reference stars used in the ground-based determinations.

stability limits given above. The results are plotted in Figure 7. Based conservatively on Figure 5, a periodic astrometric perturbation of either star with a semiamplitude larger than ~ 3 mas would have been detected. The data in Figure 7 then indicate that a companion of Procyon A of $\sim 5 M_{\text{Jup}}$ or less could escape astrometric detection. At $\sim 10 M_{\text{Jup}}$, only an orbital period longer than ~ 1.5 yr would have led to detection in our data. Progressively more massive planets orbiting Procyon A would have been detected more easily, except at the shortest orbital periods. Thus, in general, our limits are not competitive with what can be achieved with high-precision RV data (apart from orbits viewed at very low inclinations).

Our limits are more useful for Procyon B, for which a precision RV study is impractical. A $\sim 5 M_{\text{Jup}}$ companion with a period longer than ~ 2 yr is excluded, and for $\sim 10 M_{\text{Jup}}$ the lower-limit period is ~ 0.5 yr.

7. Astrophysics of Procyon A

We now turn to discussions of the astrophysical implications of our dynamical-mass results for both stellar components of Procyon. We start in this section with the primary star, Procyon A, and then discuss the WD Procyon B in §8.

7.1. Asteroseismology

With the advent of asteroseismology, Procyon A was recognized as a unique object for exploring non-radial stellar oscillations. Oscillation frequencies are particularly sensitive to boundaries between radiative and convective regions. Stars near the main sequence in the mass range near that of Procyon A are believed to exhibit a convective core, a radiative envelope, and a very thin outer convection zone (e.g., Guenther & Demarque 1993).

Helioseismology shows that diffusion of helium and heavy elements in the solar interior significantly affects the solar oscillation frequencies, and it is expected also to play a role in the radiative envelope of Procyon A. In addition, the convective core overshoot at the core’s edge must be taken into account. The amount of core overshoot in a star of this mass is not well known. It strongly affects the morphology of the evolutionary track and the evolutionary rate in the post-main-sequence phase of evolution where Procyon lies.

The oscillation spectrum of Procyon A has been obtained from ground-based radial-velocity measurements (Arentoft et al. 2008), and from intensity observations with the space mission *MOST* (see Guenther et al. 2008). A Bayesian statistical study of the asteroseismic data, based on a large grid of stellar-evolution tracks, was carried out by Guenther, Demarque, & Gruberbauer (2014; hereafter GDG14). Their tracks spanned the mass range 1.41 to 1.55 M_{\odot} . Other grid parameters (see Table 2 of GDG14) covered the following variables: (1) the helium and heavy-element contents by mass ranged from $Y = 0.26$ to 0.31 and $Z = 0.014$ to 0.031; (2) the mixing-length parameter, α , in the thin outer convection zone ranged from 1.7 to 2.5; and (3) the core-overshoot parameter, β , initially ranged from 0.0 to 1.0 times the local pressure scale height, H_p . Because of unanticipated evidence for large convective overshoot, the grid was eventually extended to β values as large as 2.0 H_p . Three quantities were selected as priors in the calculations, namely the mass of Procyon A (from G00), and its position ($\log L/L_{\odot}$ and $\log T_{\text{eff}}$) in the HR diagram (HRD; see Table 1 of GDG14).

The strongest result of the GDG14 analysis was that all of the most probable theoretical models (with or without core overshoot, with adiabatic or non-adiabatic model frequencies, with or without diffusion in the radiative envelope, and including or not including priors for the observed HRD location and mass) were found to have masses within 1σ of the mass inferred from observations of $1.497 \pm 0.037 M_{\odot}$, as published by G00. The error bar for the

most probable theoretical mass is still large, and more precise oscillation frequencies will be needed in the future to reduce it. But it is encouraging that this result is in such good agreement with the dynamical mass of $1.478 \pm 0.012 M_{\odot}$ derived from our observational analysis in the present paper.

Another result of the Bayesian analysis is relevant. The most probable models were characterized by substantial overmixing beyond the formal boundary of the convective core, with values of β as high as $1.0 H_p$ or even larger. This result exceeds the expected value of $\beta = 0.2$ or less, generally accepted for core convective overshoot in similar stars. This may be evidence for diffusive mixing beyond the standard overshoot region, as recently discussed by Moravveji et al. (2015) in the case of the more massive star KIC 10526294. A full understanding of this result will require continued seismic monitoring of Procyon A to improve the precision of the oscillation frequencies, as well as more sophisticated modeling in the overshoot region.

7.2. The Age of Procyon A

Knowing the age of Procyon A is critical to understanding the past evolution of the binary system. In conjunction with the cooling age of the companion WD, the age of Procyon A allows us to estimate the original mass of the Procyon B progenitor (see L13 and the discussion in §8.2 below).

We constructed grids of stellar evolutionary tracks for stars with the dynamical mass of $1.478 M_{\odot}$ derived in the present paper, following them from the zero-age main sequence (ZAMS) to the subgiant branch. The tracks were calculated under the assumption of single-star evolution, i.e., no interaction between Procyon A and its companion during the course of its evolution from the ZAMS to the present.

We calculated models that either include or ignore the effects of element diffusion, and for amounts of convective-overshoot efficiency at the edge of the convective core of $\beta = 0$, 0.2, and $1.0 H_p$. A standard model of convective core overshoot was adopted, as described in GDG14. The temperature gradient in the overshoot region was constrained to be the local radiative temperature gradient. This situation has been described as “overmixing,” as opposed to “penetrative convection,” where the temperature gradient is adiabatic (see Zahn 1991; GDG14). We used a near-solar metallicity of $Z = 0.02$, and adjusted the hydrogen abundance in the ZAMS starting model so as to ensure that each track passed through the Procyon A error box (from Doğan et al. 2010) in the HRD.

Figure 8 displays three of these tracks, constructed with the stellar-evolution code YREC (Demarque et al. 2008). All of these models include helium and heavy-element diffusion in the radiative envelope, using the formalism of Bahcall & Loeb (1990). Core overshoot is the major uncertainty in determining the ages of these models. The track plotted in red assumes no core overshoot ($\beta = 0$); the track in green has a standard value of core overshoot ($\beta = 0.2$); and the track in blue has large core overshoot ($\beta = 1.0$). The hydrogen contents in the ZAMS starting models were $X = 0.672$ (red track), 0.680 (green track), and 0.716 (blue track). These abundances are all consistent with accepted uncertainties in X .

The red and green tracks are morphologically similar to tracks used in previous studies of Procyon A. In particular, note Procyon A’s position just below the well-known leftward “hook,” due to core hydrogen exhaustion. This near coincidence was, until the advent of precision asteroseismology, a major source of ambiguity in identifying the precise evolutionary status of Procyon A. However, seismology clearly placed Procyon A in the core-burning phase of evolution; but as discussed above it also surprisingly revealed the presence of extensive mixing in the interior outside the convective core (see GDG14). Due

to the very large amount of overshoot, the blue track has a quite different morphology from the other two, and it also evolves more slowly. In this case, Procyon A lies well before the hydrogen-exhaustion phase.

The Procyon A ages based on the red, green, and blue tracks are 1.673, 1.817, and 2.703 Gyr. If one accepts the main results from the GDG14 Bayesian statistical analysis of the seismic data, then the preferred age is close to 2.70 Gyr. Such an age may be an upper limit. While a minimum age near 1.8 Gyr (as found by both L13 and GDG14) seems well established, there remains an uncertainty in the maximum age, which depends sensitively not only on the amount of chemical mixing from the core but also on the composition profile and structure above the core edge in the envelope. The recently published seismological study by Moravveji et al. (2015) of KIC 10526294, a $3 M_{\odot}$ star near the main sequence, shows that the frequencies observed by the *Kepler* mission can be tightly fitted to a diffusion model in the overshoot region. Improved oscillation frequencies of the same quality will be needed to produce a similar result for Procyon A. Finally, it should also be emphasized that the validity of this discussion rests upon the assumption of single-star evolution at constant mass for the A component (see below).

8. Astrophysics of Procyon B

8.1. Testing White-Dwarf Physics

Procyon B lies mostly hidden in the glare of its much brighter primary star. Virtually all that was known about it in the pre-*HST* era was based only on its astrometric properties and approximate brightness estimates. However, using *HST*, Provencal et al. (1997) acquired WFPC2 images of Procyon B in several wide- and narrow-band filters, with effective wavelengths ranging from 1600 to 7828 Å, and covering most of the star’s spectral energy

distribution (SED). From these photometric data they deduced a helium-composition photosphere, and estimated the star’s effective temperature ($T_{\text{eff}} = 8688 \pm 200$ K) and radius ($R_B = 0.0096 \pm 0.0005 R_{\odot}$). Based on the I92 astrometric mass of $0.622 \pm 0.023 M_{\odot}$, this relatively small radius called into question the assumption of the CO degenerate core that would be expected for a WD of this mass. Provencal et al. instead suggested the remarkable possibility of an iron core—placing the star in an “iron box”—as implied by the zero-temperature WD mass-radius relations of Hamada & Salpeter (1961).

The nature of Procyon B became clearer five years later when P02 used *HST* to obtain a series of Space Telescope Imaging Spectrograph (STIS) spectra, covering 1800 to 10,000 Å. These revealed the presence of C₂ Swan bands, as well as absorption features due to C I, Mg II, Ca II, and Fe I. Balmer lines are absent. Along with the earlier results, these features show the star to be a DQZ WD, i.e., having a He-dominated atmosphere, but also containing carbon (Q) and heavier metals (Z). Model-atmosphere fitting to the STIS spectra resulted in a significantly lower T_{eff} of 7740 ± 50 K, and a correspondingly larger radius of $0.01234 \pm 0.00032 R_{\odot}$, based on a V magnitude of 10.82 ± 0.03 obtained from the observed SED. This radius, along with a lowered astrometric mass of $0.602 \pm 0.015 M_{\odot}$ from G00, removed the earlier discrepancy with the mass-radius relation for CO-core WDs.

Our new dynamical mass for Procyon B allows refinement of a number of its astrophysical parameters and a stringent test of theoretical WD models. We have slightly modified the radius determined by P02, by adjusting for our adopted parallax, obtaining $R_B = 0.01232 \pm 0.00032 R_{\odot}$. In Figure 9, we compare theoretical predictions with our new parameters for Procyon B. We use theoretical modeling data from the Montreal photometric tables⁹ for WDs with pure-helium atmospheres and CO cores. The top panel in Figure 9

⁹<http://www.astro.umontreal.ca/~bergeron/CoolingModels>. These tables are based on evolutionary sequences and model atmospheres calculated by Holberg & Bergeron

shows the location of Procyon B in the theoretical HRD ($\log L/L_\odot$ vs. $\log T_{\text{eff}}$), along with the model cooling tracks for DB WDs with masses of 0.5, 0.6, and $0.7 M_\odot$. The location of Procyon B in the HRD is in excellent agreement with that expected for a WD of our dynamical mass of $0.592 \pm 0.006 M_\odot$. Also shown in the top panel of Figure 9 are isochrones for ages of 1, 1.25, and 1.5 Gyr, again based on the Montreal tables. By interpolation in the theoretical data, we estimate the cooling age of Procyon B to be 1.37 ± 0.04 Gyr.

In the bottom panel of Figure 9, we plot the position of Procyon B in the mass-radius plane. It is compared with a theoretical mass-radius relation for a He-atmosphere CO-core WD with $T_{\text{eff}} = 7740$ K, obtained through interpolation in the Montreal tables. The observed mass and radius are in excellent agreement with the theoretical relation. Also plotted is the Hamada & Salpeter (1961) mass-radius relation for zero-temperature WDs composed of ^{56}Fe , which was consistent with the parameters of Procyon B given by Provencal et al. (1997); with our revised parameters, there is no longer agreement with Fe—as first shown by P02.

The surface gravity of Procyon B (in cgs units), based on the mass and radius, is $\log g = 8.028 \pm 0.023$. Unfortunately, without Balmer lines, there are no gravity-sensitive features in the *HST* spectra that would test for consistency with this value. The predicted gravitational redshift is $30.46 \pm 0.85 \text{ km s}^{-1}$, but Procyon B possesses no detectable $\text{H}\alpha$ line from which the redshift could be measured using traditional techniques. Onofrio & Wegner (2014) have recently attempted to measure wavelength shifts in the archival *HST* spectra of Procyon B, using features of Ca II, Mg II, and C_2 . They appear to have detected the gravitational redshift, but uncertain corrections for pressure shifts are needed.

(2006), Kowalski & Saumon (2006), Tremblay et al. (2011), and Bergeron et al. (2011).

8.2. Procyon B Progenitor and the Initial-to-Final-Mass Relation

L13 made a comprehensive analysis of the existing data on Procyon A and B, aiming to determine a consistent picture of the system’s evolution. For Procyon B, L13 adopted the P02 effective temperature, but assumed a mass of $0.553 \pm 0.015 M_{\odot}$, a value $\sim 0.04 M_{\odot}$ lower than the dynamical mass determined in the present paper.¹⁰ From these parameters, L13 obtained a cooling age of 1.19 Gyr for Procyon B. Combined with the age of Procyon A, which they determined to be 1.87 Gyr from its position in the HRD, this implied a main-sequence lifetime of only 0.68 Gyr for the progenitor of the WD, corresponding to an initial mass of $2.59 M_{\odot}$. As L13 noted (their Fig. 2 and associated text and references), these results placed Procyon B significantly below the initial-to-final-mass relation (IFMR) established from studies of WDs in open clusters. A $2.59 M_{\odot}$ progenitor would be expected to produce a WD with a mass of about $0.69 M_{\odot}$ (cf. Ferrario et al. 2005).

As discussed in §7.2, the age of Procyon A may be considerably greater than adopted by L13. This is the case if we use the evolutionary track with large core overshoot, as favored by the GDG14 seismologic analysis. For a Procyon A age of 2.70 Gyr, and our cooling age of 1.37 Gyr for the WD, the main-sequence lifetime of the progenitor of Procyon B was 1.33 Gyr. This corresponds to a ZAMS mass of about $2.2 M_{\odot}$ (if the progenitor had a large core overshoot of $\beta = 1.0$ like Procyon A), or a lower initial mass of about $1.9 M_{\odot}$ (if it had a “normal” overshoot of $\beta = 0.2$). The Ferrario et al. (2005) IFMR predicts WD masses of 0.65 or $0.625 M_{\odot}$ for such initial masses. Thus there remains a discrepancy, albeit smaller than found by L13, and within the cosmic scatter in the relation (e.g., Fig. 2 in L13).

¹⁰The lower mass used by L13 was from a 2012 private communication from G.H.S. and H.E.B.; at that time we still had not done the rigorous astrometry of our *HST* images described in the present paper, and also were using the smaller value of a_A from I92.

If future observations force an unlikely revision in the current interpretation of the seismic data, Procyon A’s age could in principle be as low as ~ 1.8 Gyr, resulting in an initial mass possibly as high as about $3 M_{\odot}$ for Procyon B—and a much more severe disagreement with the mean IFMR.

8.3. Atmospheric Carbon and Heavy Elements

Procyon B presents an unusual case of a WD with the rare DQZ spectral type being a companion of a main-sequence (or slightly evolved) star. A somewhat similar system, HR 637 (GJ 86), was recently studied by Farihi et al. (2013). The K0 V primary in this binary is orbited in a 15.9-day period by a Jovian planet of perhaps $4.4\text{--}4.7 M_{\text{Jup}}$, detected through RV measurements (Queloz et al. 2000). The K dwarf also has a WD companion in a more distant orbit, with a period estimated at several hundred years. Farihi et al. used *HST*/STIS to obtain spectra of the resolved WD companion. They found it to be He-rich, with C_2 absorption bands (spectral type DQ6), and having a remarkably similar temperature, mass, and atmospheric carbon content to those of Procyon B. The carbon in cool DQ atmospheres is likely intrinsic to the star. However, the heavier metals (e.g., Ca, Mg, and Fe) seen in Procyon B, but not in HR 637 B, are probably accreted from an external source.

The source of heavy elements accreting onto the photospheres of single DA and DB WDs is usually considered to be a circumstellar debris disk, composed of rocky material (e.g., Jura 2003). Such disks likely form when the WD tidally disrupts terrestrial planets, asteroids, or planetesimals. Although no heavy elements were observed in HR 637 B, Farihi et al. discussed their presence in Procyon B. They examined the heavy-element accretion rates necessary to account for the abundances of Ca and Mg in the Procyon B photosphere, along with the lack of hydrogen, and ruled out accretion from the interstellar medium

or a stellar wind from Procyon A. They instead argued for a circumstellar disk around Procyon B as the heavy-element source.

Such a debris disk would be very compact, within a few tenths of a solar radius, and not significantly influenced by the gravity of Procyon A. The object(s) that formed the disk were unlikely to have originated in a protoplanetary disk around the Procyon B precursor, since planet formation would have been confined to within ~ 2.3 AU (Holman & Wiegert 1999), and any such planetesimals would likely have been destroyed during the red-giant phases. Instead, Farihi et al. argue that the reservoir could be a much larger disk enclosing the entire binary. They also conclude that it was unlikely that any Jovian-mass objects ever formed around either Procyon A or B, since their formation would have been confined to within the snow limits of each star. This is certainly consistent with the lack of any dynamical evidence for existence of ~ 5 to $10 M_{\text{Jup}}$ third bodies, as reported in our §6.

Another alternative is that the polluting material results from “second-generation” planets, as described by Perets & Kenyon (2013). They suggest that a portion of the wind from an AGB star may be captured by a binary companion (in this case, Procyon A), creating a disk in which planets may form. However, in order to pollute the WD atmosphere, an asteroid or planetesimal born in this disk would then have to be ejected from its orbit around A and into the vicinity of Procyon B.

9. Past Evolution of the Procyon System

The discussion in the previous two sections treated both components of the Procyon system as if they have evolved as single stars. Such an analysis does lead to a reasonably consistent picture, with a primary star whose position in the HRD can be reproduced with theoretical tracks based on the star’s observed mass (although with indications of unusually

efficient core overshoot), and a reasonably well-behaved WD companion (although with hints that its mass is somewhat lower than expected).

The periastron separation of A and B in the present-day orbit is 9.1 AU. If the progenitor of B had a mass of $\sim 2.2 M_{\odot}$, as deduced in the previous section, then the total mass of the system was reduced from $\sim 3.7 M_{\odot}$ to its present value of $2.07 M_{\odot}$ due to evolutionary mass loss from the progenitor. Under the assumption that the mass loss was on a timescale slow compared to the orbital period (cf. Burleigh et al. 2002, §2), this implies that the periastron separation of the pair was only ~ 5.1 AU in the progenitor system.

At such a minimum separation, the progenitor was likely to have avoided Roche-lobe overflow. This is consistent with the high orbital eccentricity (0.40) in the present system, which appears to rule out a phase in which the two stars shared a common envelope (during the giant or AGB phase of the initial B component), because it would have led to rapid circularization of the orbit—if not a spiralling down to a shorter period or even a merger. The high eccentricity thus sets indirectly an upper limit on the initial mass of Procyon B. However, the eccentricity may have favored strong periodic tidal interaction at times of closest approach between the two stars. The unusually large mixing detected by seismology could then be the result of such tidal interaction.

A more extreme interaction may have occurred during wind mass loss from the B progenitor when it was a red giant or AGB star, and during ejection of a planetary nebula. This may have led to mass transfer from the WD progenitor onto Procyon A (see Wegner 1973; Fuhrmann et al. 2014)—in addition to the hypothetical disk and second-generation planet formation around A discussed in the preceding section. Thus the original Procyon A could have been less massive than at present, and therefore more slowly evolving. The main effect of accretion would have been to speed up the rate of evolution of Procyon A from that of a lower-mass star to its rate at the present time.

10. Summary

Based on our analysis of two decades of precise astrometry of the Procyon system with the *Hubble Space Telescope*, combined with historical measurements dating back to the 19th century, we have derived dynamical masses for both components. The F5 subgiant Procyon A is found to have a mass of $1.478 \pm 0.012 M_{\odot}$, and the Procyon B white-dwarf companion has a mass of $0.592 \pm 0.006 M_{\odot}$. We find no evidence for perturbations due to third bodies in the system, at levels down to about $5\text{--}10 M_{\text{Jup}}$.

The mass of Procyon A is in excellent agreement with theoretical predictions based on asteroseismology and its position in the H-R diagram. However, a surprisingly high amount of core convective overshoot, compared with that usually adopted for individual stars and stars in open star clusters, is required to achieve this agreement. If correct, this implies that the age of Procyon A is about 2.7 Gyr.

The position of Procyon B in the H-R diagram is in excellent agreement with a theoretical cooling track for a white dwarf of its measured mass, and implies a cooling age of 1.37 Gyr. In the mass-radius plane, Procyon B’s location is in agreement with theoretical predictions for a carbon-oxygen white dwarf with a helium-dominated atmosphere. The mass of its progenitor, if the age of A is 2.7 Gyr, was about $1.9 M_{\odot}$ if the progenitor had a “normal” amount of core overshoot, or about $2.2 M_{\odot}$ if it had a larger amount similar to that of A. In either case, the mass of the white dwarf is lower than expected based on the mean initial-to-final-mass relation for single stars in open clusters, although still within the cosmic scatter.

Although treating both stars as if they have evolved separately leads to a fairly consistent interpretation of the system, we point out that in the progenitor system the two stars were actually relatively close to each other (≈ 5 AU) at every periastron passage. Thus the stars may have been affected by tidal interactions and even mass capture from

a red-giant wind, and their actual evolutionary histories may have been much more complicated than the simple picture presented here.

Support was provided by NASA through grants from the Space Telescope Science Institute, which is operated by the Association of Universities for Research in Astronomy, Inc., under NASA contract NAS5-26555. J.B.H. acknowledges support from NSF grant AST-1413537. We are grateful to Elliott Horch for help in verifying the orbit fit to the photographic data, and to Peter Eggleton, David Guenther, and Bill van Altena for several helpful discussions.

Facilities: *HST* (WFPC2, WFC3)

REFERENCES

- Allende Prieto, C., Asplund, M., García López, R. J., & Lambert, D. L. 2002, *ApJ*, 567, 544
- Arentoft, T., Kjeldsen, H., Bedding, T. R., et al. 2008, *ApJ*, 687, 1180
- Auwers, A. 1873, *MNRAS*, 34, 25
- Bahcall, J. N., & Loeb, A. 1990, *ApJ*, 360, 267
- Barnard, E. E. 1913, *AJ*, 27, 193
- Bergeron, P., Wesemael, F., Dufour, P., et al. 2011, *ApJ*, 737, 28
- Bessel, F. W. 1844, *MNRAS*, 6, 136
- Bevington, P. R. 1969, *Data Reduction and Error Analysis for the Physical Sciences* (New York: McGraw-Hill).
- Bond, G. 1862, *Astronomische Nachrichten*, 57, 131
- Burleigh, M. R., Clarke, F. J., & Hodgkin, S. T. 2002, *MNRAS*, 331, L41
- Chiavassa, A., Bigot, L., Kervella, P., et al. 2012, *A&A*, 540, A5
- Davis, C. H. 1876, *Astronomische Nachrichten*, 87, 241
- Demarque, P., & Guenther, D. B. 1988, in *Advances in Helio- and Asteroseismology*, IAU Symp. 187, ed. J. Christensen-Dalsgaard & S. Frandsen (Dordrecht: Reidel), 287
- Demarque, P., Guenther, D. B., Li, L. H., Mazumdar, A., & Straka, C. W. 2008, *Ap&SS*, 316, 31
- Doğan, G., Bonanno, A., Bedding, T. R., et al. 2010, *Astronomische Nachrichten*, 331, 949
- Farihi, J., Bond, H. E., Dufour, P., et al. 2013, *MNRAS*, 430, 652
- Ferrario, L., Wickramasinghe, D., Liebert, J., & Williams, K. A. 2005, *MNRAS*, 361, 1131
- Fuhrmann, K., Chini, R., Buda, L.-S., & Pozo Nuñez, F. 2014, *ApJ*, 785, 68

- Gatewood, G., & Han, I. 2006, *AJ*, 131, 1015
- Gilliland, R. L. 2005, Instrument Science Report TEL 2005-02 (Baltimore, MD: STScI)
- Gilliland, R. L., Nugent, P. E., & Phillips, M. M. 1999, *AJ*, 521, 30
- Gilliland, R. L., Rajan, A., & Deustua, S. 2010, Instrument Science Report WFC3 2010-10 (Baltimore, MD: STScI)
- Girard, T. M., Wu, H., Lee, J. T., et al. 2000, *AJ*, 119, 2428 (G00)
- Gonzaga, S., & Biretta, J. 2010, HST WFPC2 Data Handbook, Version 5.0 (Baltimore: STScI)
- Goudfrooij, P., Bohlin, R. C., Maíz-Apellániz, J., & Kimble, R. A. 2006, *PASP*, 118, 1455
- Gray, R. O., Napier, M. G., & Winkler, L. I. 2001, *AJ*, 121, 2148
- Guenther, D. B., & Demarque, P. 1993, *ApJ*, 405, 298
- Guenther, D. B., Demarque, P., & Gruberbauer, M. 2014, *ApJ*, 787, 164 (GDG14)
- Guenther, D. B., Kallinger, T., Gruberbauer, M., et al. 2008, *ApJ*, 687, 1448
- Hamada, T., & Salpeter, E. E. 1961, *ApJ*, 134, 683
- Hartmann, L., Garrison, L. M., Jr., & Katz, A. 1975, *ApJ*, 199, 127
- Holberg, J. B., & Bergeron, P. 2006, *AJ*, 132, 1221
- Holman, M. J., & Wiegert, P. A. 1999, *AJ*, 117, 621
- Innis, J. L., Isaak, G. R., Speake, C. C., et al. 1994, *MNRAS*, 271, 573
- Irwin, A. W., Fletcher, J. M., Yang, S. L. S., Walker, G. A. H., & Goodenough, C. 1992, *PASP*, 104, 489 (I92)
- Janson, M., Bonavita, M., Klahr, H., et al. 2011, *ApJ*, 736, 89
- Johnson, H. L., & Morgan, W. W. 1953, *ApJ*, 117, 313

- Jura, M. 2003, *ApJ*, 584, L91
- Kervella, P., Thévenin, F., Morel, P., et al. 2004, *A&A*, 413, 251
- Kowalski, P. M., & Saumon, D. 2006, *ApJ*, 651, L137
- Kozhurina-Platais, V. 2014, Instrument Science Report WFC3 2014-12 (Baltimore, MD: STScI)
- Kuiper, G. P. 1937, *ApJ*, 85, 253
- Liebert, J., Fontaine, G., Young, P. A., Williams, K. A., & Arnett, D. 2013, *ApJ*, 769, 7 (L13)
- Moravveji, E., Aerts, C., Pápics, P. I., Triana, S. A., & Vandoren, B. 2015, *A&A*, 580, A27
- Mosser, B., Bouchy, F., Martić, M., et al. 2008, *A&A*, 478, 197
- Onofrio, R., & Wegner, G. A. 2014, *ApJ*, 791, 125
- Perets, H. B., & Kenyon, S. J. 2013, *ApJ*, 764, 169
- Press, W. H., Teukolsky, S. A., Vetterling, W. T., & Flannery, B. P. 1992, *Numerical Recipes in Fortran: The Art of Scientific Computing*, 2nd ed. (Cambridge: Cambridge Univ. Press)
- Provencal, J. L., Shipman, H. L., Koester, D., Wesemael, F., & Bergeron, P. 2002, *ApJ*, 568, 324 (P02)
- Provencal, J. L., Shipman, H. L., Wesemael, F., et al. 1997, *ApJ*, 480, 777
- Queloz, D., Mayor, M., Weber, L., et al. 2000, *A&A*, 354, 99
- Schaeberle, J. M. 1896, *PASP*, 8, 314
- Schaeberle, J. M. 1897, *AJ*, 17, 76
- Schroeder, D. J., Golimowski, D. A., Brukardt, R. A., et al. 2000, *AJ*, 119, 906
- See, T. J. J. 1898, *AJ*, 19, 57

- Spencer Jones, H. 1928, MNRAS, 88, 403
- Steffen, M. 1985, A&AS, 59, 403
- Straka, C. W., Demarque, P., & Guenther, D. B. 2005, ApJ, 629, 1075
- Strand, K. A. 1951, ApJ, 113, 1 (S51)
- Struve, O. 1874, MNRAS, 34, 335
- Tremblay, P.-E., Bergeron, P., & Gianninas, A. 2011, ApJ, 730, 128
- van Leeuwen, F. 2007, A&A, 474, 653
- Wegner, G. 1973, MNRAS, 165, 271
- Zahn, J.-P. 1991, A&A, 252, 179

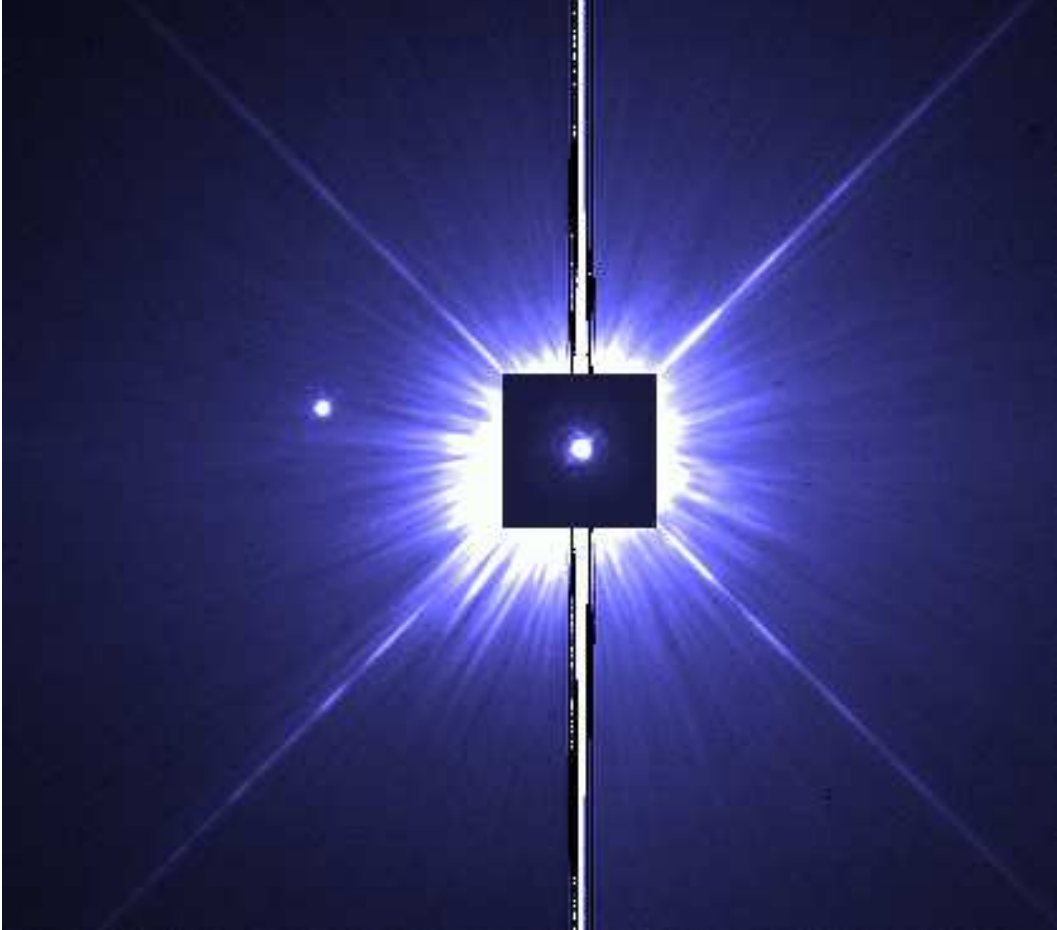


Fig. 1.— False-color *HST* WFPC2 image of Procyon, from frames obtained in the near-ultraviolet F218W filter on 1997 November 27. An inset showing the unsaturated Procyon A from a 0.14-s exposure is superposed on a 100-s exposure, taken at the same telescope pointing. The white dwarf Procyon B is easily resolved, at a separation of $4''.706$. In the near ultraviolet the measured brightness difference is 8.5 mag.

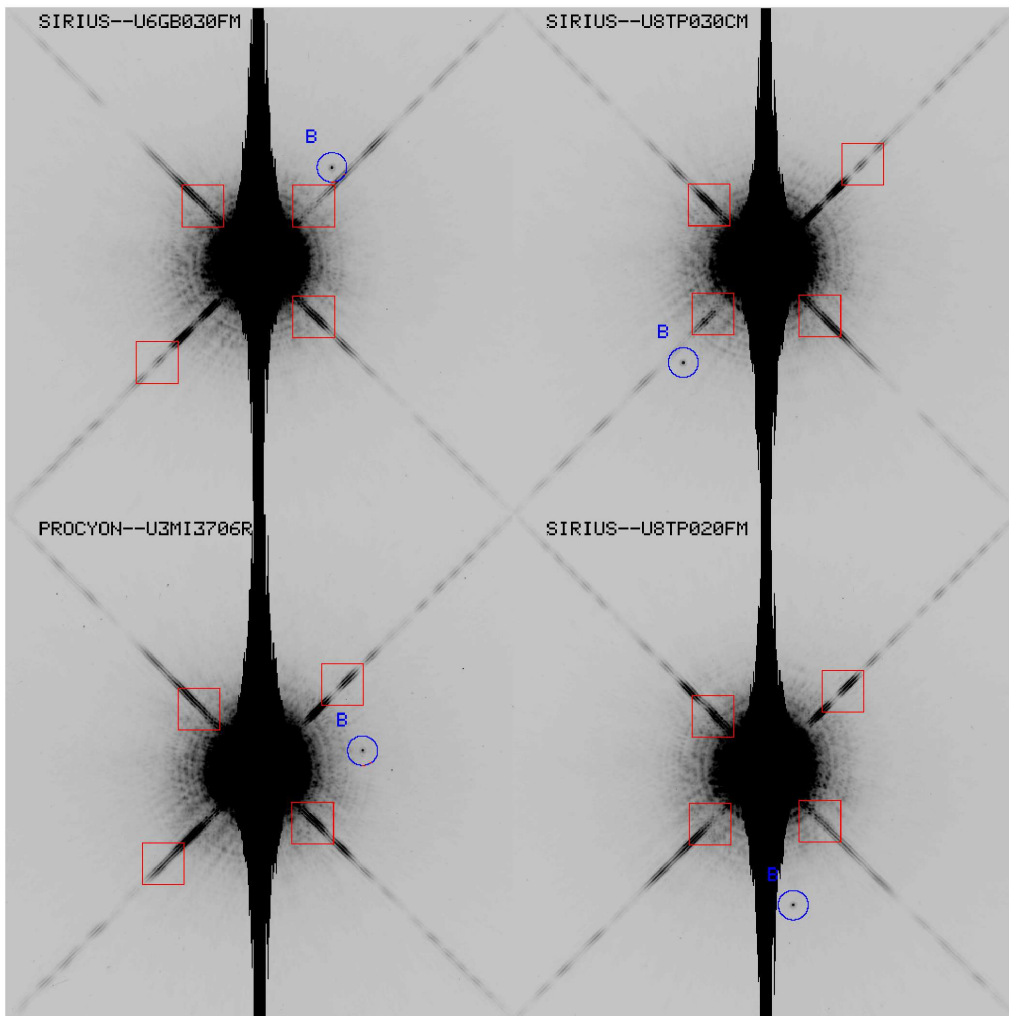


Fig. 2.— Each of these four subpanels shows a 512×512 pixel region from WFPC2 images, centered on either Procyon A or Sirius A, with specific image numbers indicated within the figure. These $23'' \times 23''$ frames show the strongly oversaturated A at center, with the much fainter B component circled and labeled. The red boxes indicate the regions within each diffraction spike that were used to determine the centroid location of A; see text for details.

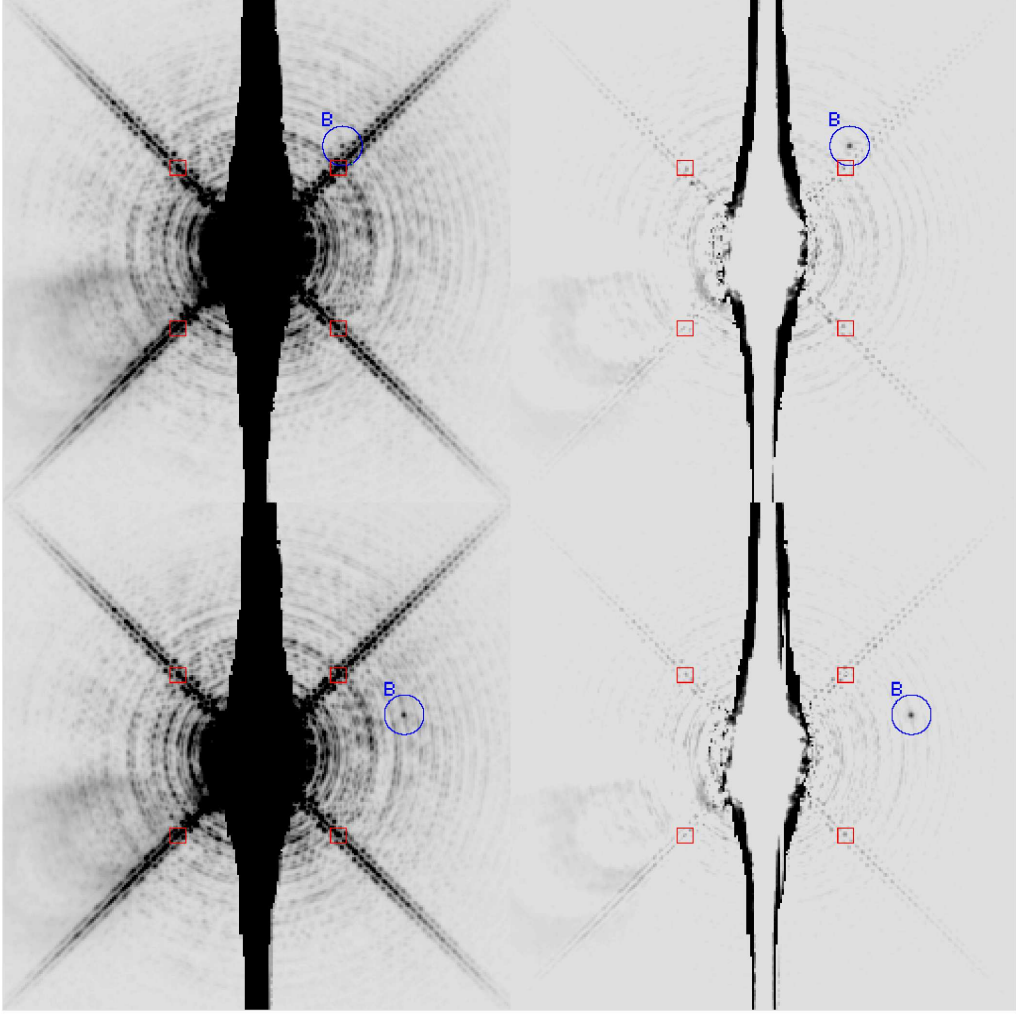


Fig. 3.— The upper two images show 256×256 pixel ($10''.1 \times 10''.1$) regions centered on Procyon A from a WFC3 frame (ibk701010) obtained on 2011 Feb 7, and the lower two images show Procyon A from another frame (ibti01010) taken on 2012 Mar 9. The two left-hand panels are the direct images, while the right-hand panels are after a best-fit representation of the over-sampled saturated PSF has been subtracted. The red squares indicate the regions on the diffraction spikes that were used to fix the PSF centroid, while the location of Procyon B is circled and labeled.

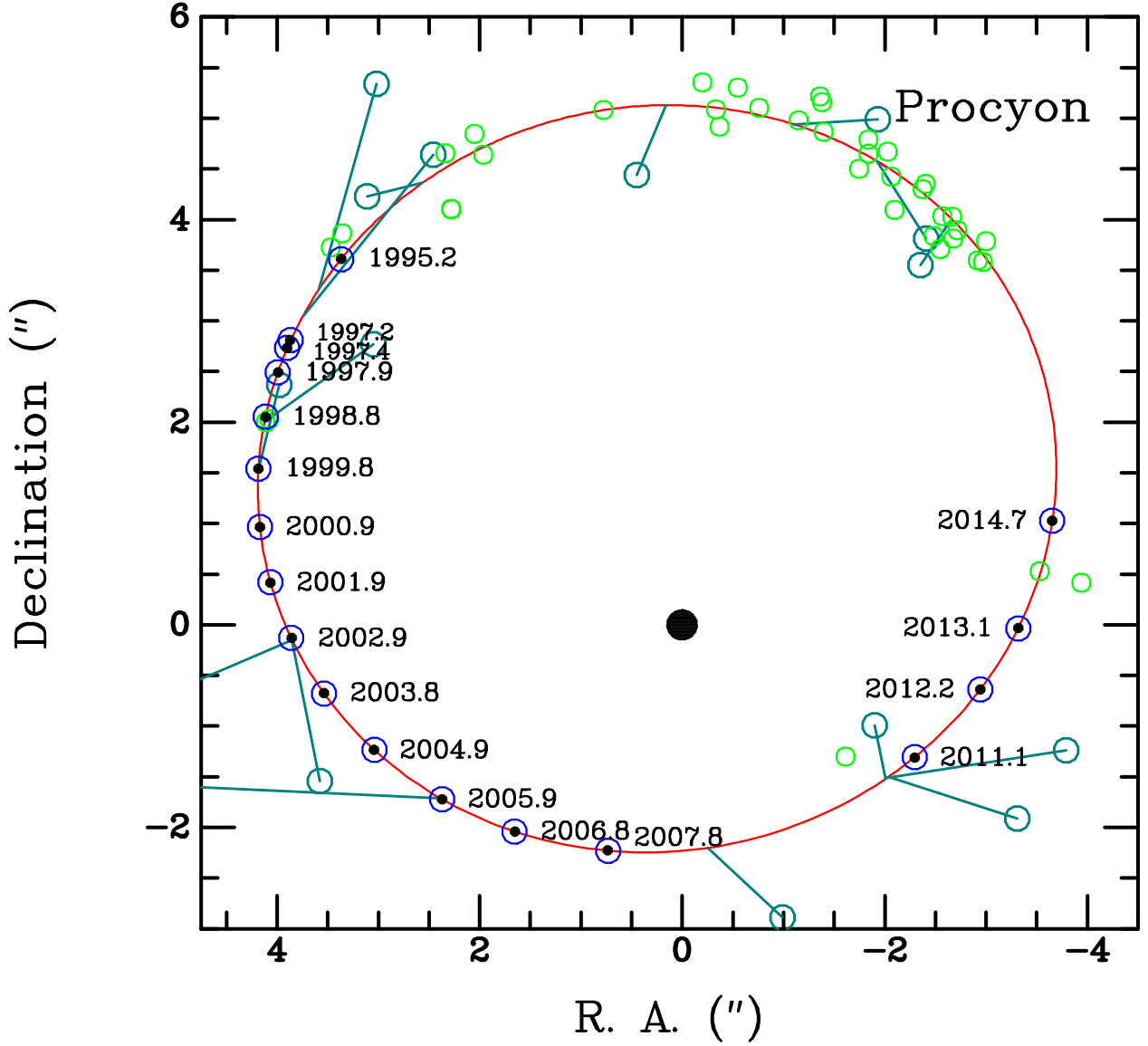


Fig. 4.— The relative orbit of Procyon B. *HST* observations from Table 3 are plotted as *small filled black circles*. The culled ground-based observations from Table 7 are shown as *open green circles*. Ground-based measurements that were rejected from our solution are plotted as *open turquoise circles*, connected by straight lines to their predicted locations. The *solid red curve* is our fit to the visual orbit, using the elements listed in Table 8. *Open blue circles* mark the positions predicted from our orbital elements at the dates of the *HST* observations, indicated in the labels.

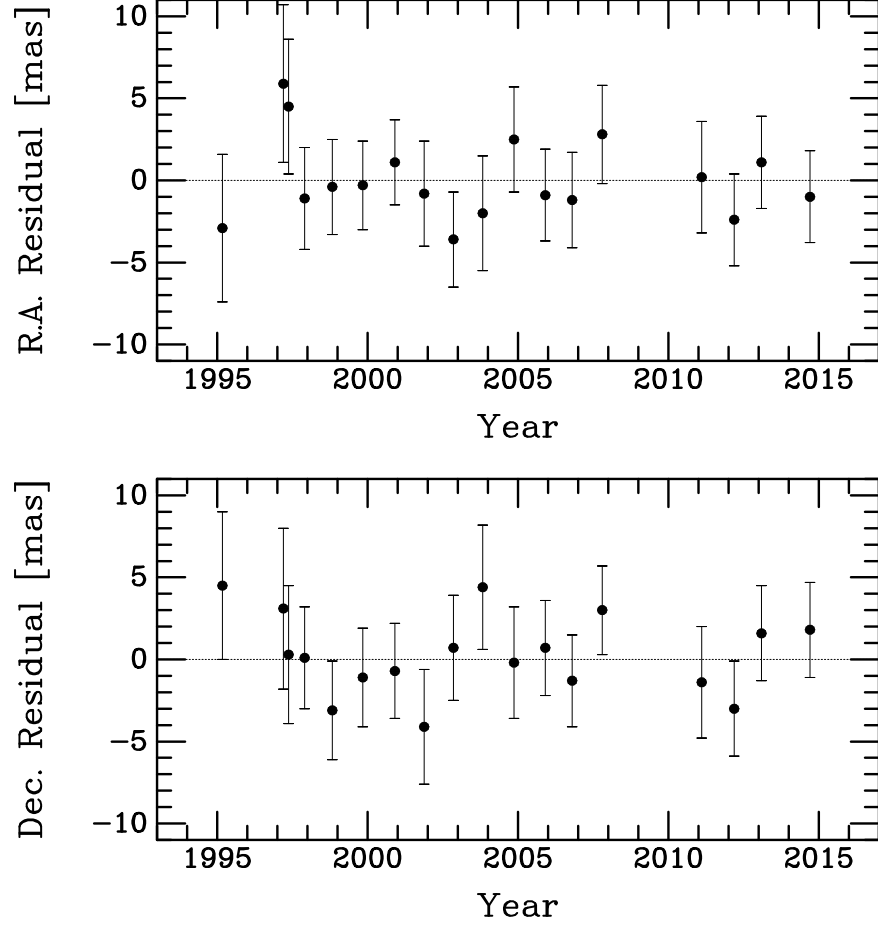


Fig. 5.— Residuals (in milliarcseconds) between the right-ascension (**top panel**) and declination (**bottom panel**) position offsets of Procyon B from Procyon A observed with *HST*, and the offsets predicted by our adopted orbital elements.

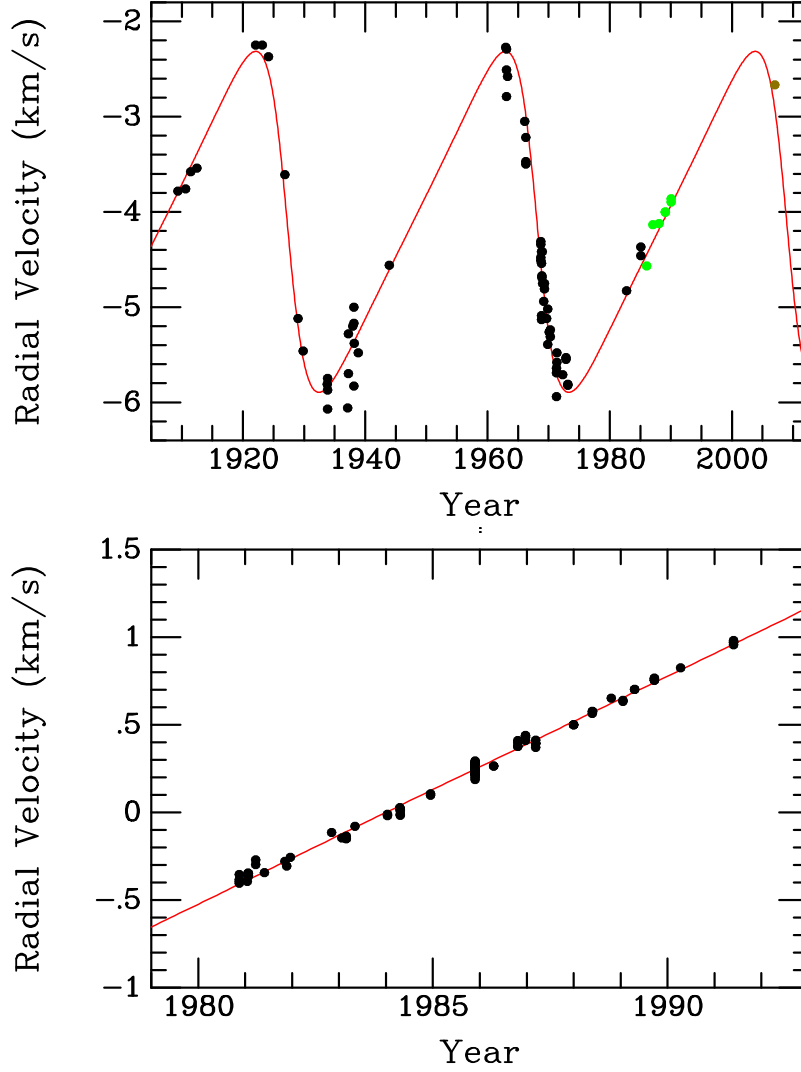


Fig. 6.— **Top:** The *red line* plots the radial-velocity curve of Procyon A that is predicted by our orbital elements, the semimajor axis of A’s astrometric motion, and the parallax, with a center-of-mass offset of -4.115 km s^{-1} . *Filled black circles* are velocity measurements on an absolute scale published by Irwin et al. (1992). *Filled green circles* are relative velocities measured by Innis et al. (1994), who shifted their zero-point to match that of Irwin et al. *Filled brown circle* is an absolute velocity measured by Mosser et al. (2008). **Bottom:** *Filled black circles* are precise relative velocity measurements (Irwin et al. 1992). The *red line* is our predicted velocity curve, shifted vertically to match the observations in the mean. In both panels our predictions—based only on astrometry—match the radial-velocity observations extremely well.

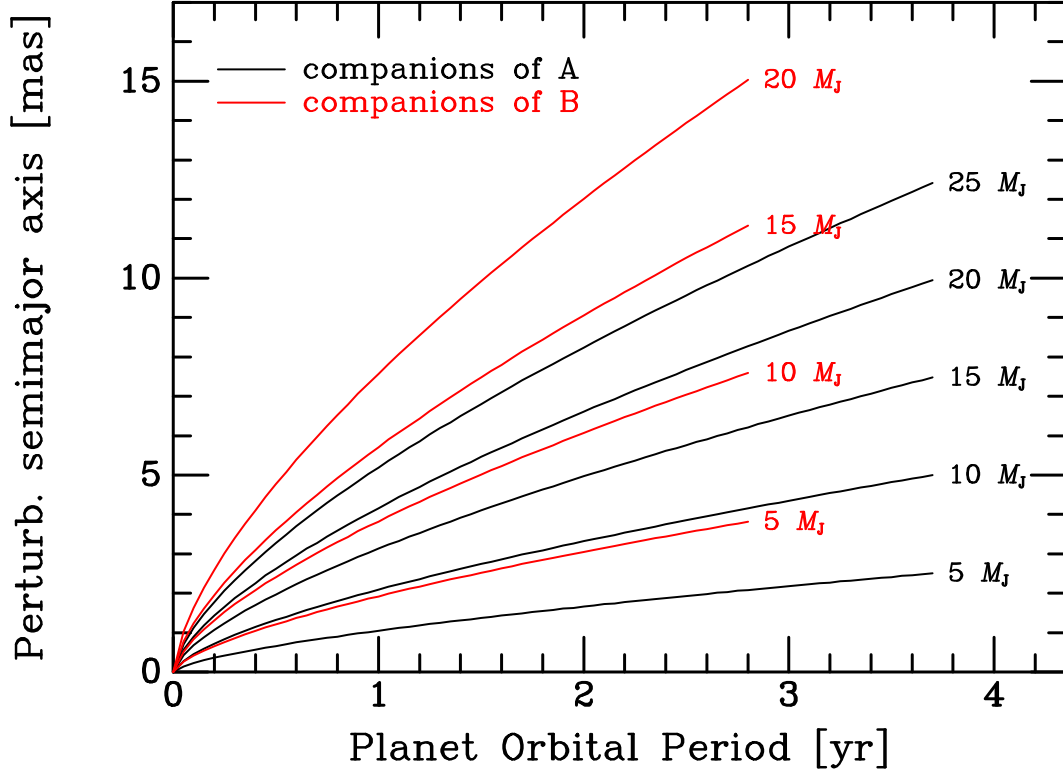


Fig. 7.— Astrometric perturbations that would result from planetary companions of Procyon A (*black curves*) or Procyon B (*red curves*), with the masses of the perturbers (in units of the mass of Jupiter) indicated in the labels. Calculations were made for periods up to the orbital-stability limits of planets with orbital periods of ~ 3.7 yr (companions of Procyon A) or ~ 2.8 yr (companions of Procyon B). The y -axis is the semimajor axis of the astrometric perturbation in milliarcseconds.

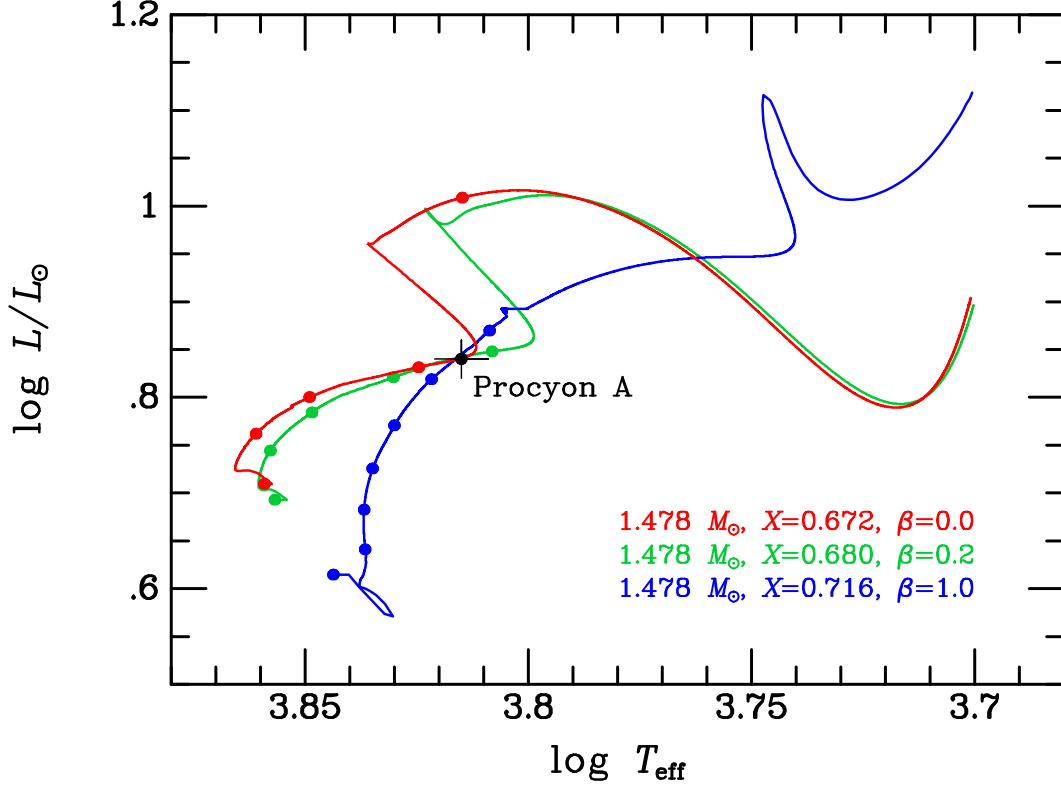


Fig. 8.— Theoretical evolutionary tracks in the H-R diagram for stars of $1.478 M_{\odot}$ and three different values of the core-overshoot parameter β : 0.0 (red curve), 0.2 (green curve), and 1.0 (blue curve). The hydrogen contents, X , have been adjusted for each track so that it passes through the location of Procyon A, marked with a black dot and error bars. The dots on each curve are located at ages in steps of 0.5 Gyr, starting at age zero on the ZAMS at the lower left. For the blue curve, favored by seismic analysis, the age of Procyon A is 2.70 Gyr.

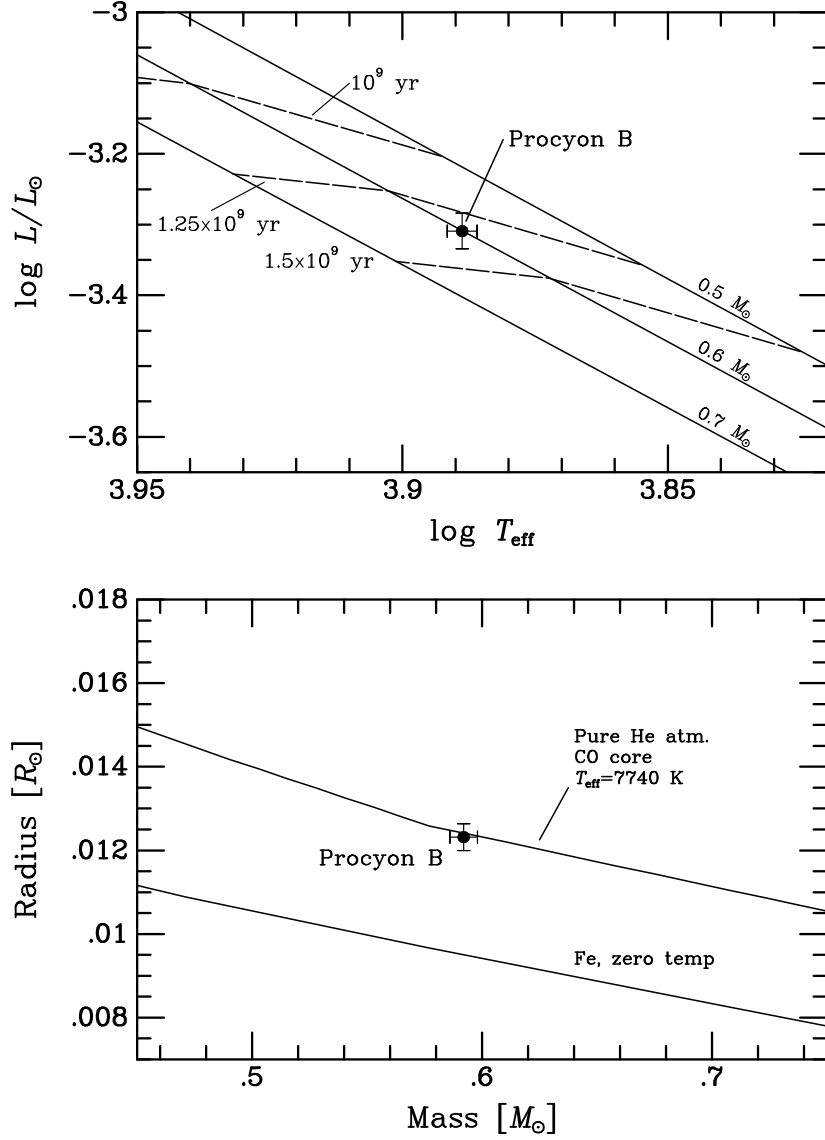


Fig. 9.— Comparisons of white-dwarf theory with the observed parameters of Procyon B. **Top:** Observed position of Procyon B in the theoretical HR diagram, compared with Montreal cooling tracks and isochrones for pure He-atmosphere CO-core white dwarfs of the indicated masses. **Bottom:** Observed position of Procyon B in the mass-radius plane, compared with a theoretical relation for pure He-atmosphere CO white dwarfs of effective temperature $T_{\text{eff}} = 7740$ K, based on the Montreal tracks. Also plotted is the mass-radius relation for a zero-temperature white dwarf composed of iron (Hamada & Salpeter 1961). In both diagrams, the agreement of theory with observations is excellent, verifying that Procyon B is a CO-core white dwarf.

Table 1. *HST* WFPC2 Observing Log for Procyon

UT Date	Filter	Dataset ^a	Exposure Times [s]	No. Pairs Or Frames ^b	Proposal ID	P. I.
1995-03-05	F218W	u2my0101t	0.11, 160	1	5374	H. Shipman ^c
1997-03-12	F1042M	u3mi3702r	18–200	6	6887	H. Ford
1997-05-17	F1042M	u3mi3802r	18–200	5	6887	H. Ford
1997-11-27	F218W	u42k0105r	0.14, 100	2	7497	H.E.B.
1998-10-29	F218W	u42k0801r	0.12, 100	4	7497	H.E.B.
1999-11-01	F218W	u59h0101r	0.11, 100–200	6	8396	H.E.B.
2000-11-28	F218W	u67h5101r	0.11, 160–200	5	8586	H.E.B.
2001-11-19	F218W	u6iz0101m	0.11, 160–200	5	9227	H.E.B.
2002-11-08	F218W	u8ip0101m	0.11, 160–200	5	9332	H.E.B.
2003-10-27	F218W	u8rm0101m	0.11, 160–200	5	9887	H.E.B.
2004-11-11	F218W	u9290101m	0.11, 160–200	5	10112	H.E.B.
2005-11-26	F218W	u9d30101m	0.11, 160–200	5	10481	H.E.B.
2006-10-21	F218W	u9o50101m	0.11, 160–200	5	10914	H.E.B.
2007-10-20	F218W	ua0p0101m	0.11, 160–200	5	11296	H.E.B.

^aDataset identifier for the first observation made at each visit.

^bNumber of usable F218W short- and long-exposure pairs at same telescope pointing made during each visit; for the F1042M images, this is the total number of single frames.

^cThe short exposure was added to Shipman’s program in response to a Director’s Discretionary request submitted by R.L.G.

Table 2. *HST* WFC3 Observing Log for Procyon

UT Date	Filter	Dataset ^a	Total Exposure [s]	No. Frames ^b	Proposal ID ^c
2010-02-24	F953N	ib7j01010 ^d	96	8	11786
2010-02-24	F953N	ib7j01020 ^d	288	8	11786
2010-02-24	F953N	ib7j01030 ^d	96	8	11786
2010-02-24	F953N	ib7j01040 ^d	288	8	11786
2011-02-07	F953N	ibk701010	608	16	12296
2011-02-07	F953N	ibk701020	608	16	12296
2012-03-09	F953N	ibt01010	608	16	12673
2012-03-09	F953N	ibt01020	608	16	12673
2013-02-03	F953N	ic1k01010	608	16	13062
2013-02-03	F953N	ic1k01020	608	16	13062
2014-09-14	F953N	ica101010	576	16	13468
2014-09-14	F953N	ica101020	576	16	13468

^aDataset identifiers for the drizzle-combined images obtained during each visit.

^bNumber of individual dithered sub-exposures contributing to the drizzle-combined frames.

^cH.E.B. was Principal Investigator for all of these programs.

^dThe 2010 observations are listed for completeness, but were not used in our analysis (see text).

Table 3. *HST* Astrometric Measurements of Procyon B Relative to A

UT Date	Besselian Date	Separation [arcsec]	J2000 Position Angle [°]	Source
1995-03-05	1995.1745	4.9389 ± 0.0044	42.977 ± 0.053	WFPC2 F218W PSF fit
1997-03-12	1997.1958	4.7851 ± 0.0047	53.997 ± 0.059	WFPC2 F1042M spike fit
1997-05-17	1997.3747	4.7651 ± 0.0040	55.022 ± 0.051	WFPC2 F1042M spike fit
1997-11-27	1997.9072	4.7058 ± 0.0030	58.027 ± 0.039	WFPC2 F218W PSF fit
1998-10-29	1998.8257	4.5973 ± 0.0028	63.499 ± 0.038	WFPC2 F218W PSF fit
1999-11-01	1999.8342	4.4583 ± 0.0027	69.771 ± 0.039	WFPC2 F218W PSF fit
2000-11-28	2000.9093	4.2809 ± 0.0026	76.977 ± 0.039	WFPC2 F218W PSF fit
2001-11-19	2001.8839	4.0859 ± 0.0032	84.147 ± 0.049	WFPC2 F218W PSF fit
2002-11-08	2002.8537	3.8584 ± 0.0029	91.939 ± 0.047	WFPC2 F218W PSF fit
2003-10-27	2003.8220	3.5988 ± 0.0035	100.787 ± 0.060	WFPC2 F218W PSF fit
2004-11-11	2004.8629	3.2840 ± 0.0032	112.092 ± 0.060	WFPC2 F218W PSF fit
2005-11-26	2005.9040	2.9293 ± 0.0027	125.956 ± 0.058	WFPC2 F218W PSF fit
2006-10-21	2006.8046	2.6266 ± 0.0027	140.997 ± 0.065	WFPC2 F218W PSF fit
2007-10-20	2007.8011	2.3452 ± 0.0027	161.715 ± 0.074	WFPC2 F218W PSF fit
2011-02-07	2011.1040	2.6431 ± 0.0047	240.339 ± 0.105	WFC3 F953N PSF fit
2012-03-09	2012.1877	3.0130 ± 0.0040	257.721 ± 0.078	WFC3 F953N PSF fit
2013-02-03	2013.0947	3.3154 ± 0.0040	269.417 ± 0.071	WFC3 F953N PSF fit
2014-09-14	2014.7038	3.7986 ± 0.0040	285.719 ± 0.062	WFC3 F953N PSF fit
2011-02-07	2011.1040	2.6381 ± 0.0048	240.205 ± 0.106	WFC3 F953N spike fit
2012-03-09	2012.1877	3.0144 ± 0.0040	257.752 ± 0.078	WFC3 F953N spike fit
2013-02-03	2013.0947	3.3166 ± 0.0040	269.447 ± 0.071	WFC3 F953N spike fit
2014-09-14	2014.7038	3.7946 ± 0.0040	285.723 ± 0.063	WFC3 F953N spike fit
2011-02-07	2011.1040	2.6406 ± 0.0034	240.272 ± 0.074	WFC3 F953N average
2012-03-09	2012.1877	3.0137 ± 0.0028	257.737 ± 0.055	WFC3 F953N average

Table 3—Continued

UT Date	Besselian Date	Separation [arcsec]	J2000 Position Angle [°]	Source
2013-02-03	2013.0947	3.3160 ± 0.0028	269.432 ± 0.050	WFC3 F953N average
2014-09-14	2014.7038	3.7966 ± 0.0028	285.721 ± 0.044	WFC3 F953N average

Table 4. *HST* WFPC2 F1042M Frames used for PSF Studies^a

Target	UT Date	Dataset ^b	Exposure Times [s]	No. Frames	Proposal ID	P. I.
Sirius	1997-03-19	u3mi1503r	12–100	4	6887	H. Ford
Sirius	1997-05-18	u3mi1603m	12–100	4	6887	H. Ford
Sirius	2001-10-27	u6gb0202m	4–35	10	9072	H.E.B.
Sirius	2002-05-10	u6gb0306m	4–60	10	9072	H.E.B.
Sirius	2002-10-20	u8if0206m	8–60	10	9334	H.E.B.
Sirius	2003-04-18	u8if0306m	8–60	10	9334	H.E.B.
Sirius	2003-10-15	u8tp0206m	8–60	10	9964	H.E.B.
Sirius	2004-08-15	u8tp0301m	8–60	12	9964	H.E.B.
Sirius	2005-04-20	u8tp0601m	8–60	12	9964	H.E.B.
Sirius	2006-01-15	u9bv0101m	8–60	12	10619	H.E.B.
Sirius	2006-12-27	u9o60101m	8–60	13	10990	H.E.B.
Sirius	2008-01-03	u9z80101m	8–60	12	11290	H.E.B.
109 Vir	2008-04-06	ub080101m	0.23–600	3	11509	R.L.G.

^aFor PSF definition to be used in centroiding B, only the Sirius exposures longer than 30 s were used, along with the 0.23-s exposures of 109 Vir.

^bDataset identifier for the first observation made at each visit.

Table 5. *HST* WFC3 F953N Frames used for PSF Studies

Target	UT Date	Dataset	Total Exposure [s]	No. Exposures ^a	Proposal ID ^b
Sirius	2010-09-02	ibk703010	48	8	12296
Sirius	2010-09-02	ibk703020	96	8	12296
Sirius	2010-09-02	ibk703030	24	4	12296
Sirius	2010-09-02	ibk703040	96	8	12296
Sirius	2011-10-01	ibt03010	48	8	12673
Sirius	2011-10-01	ibt03020	96	8	12673
Sirius	2011-10-01	ibt03030	24	4	12673
Sirius	2011-10-01	ibt03040	96	8	12673
HD 23886	2012-02-17	ibs001010	20	4	12598
HD 23886	2012-02-17	ibs001020	2524	4	12598
Sirius	2012-09-26	ic1k03010	48	8	13062
Sirius	2012-09-26	ic1k03020	96	8	13062
Sirius	2012-09-26	ic1k03030	24	4	13062
Sirius	2012-09-26	ic1k03040	96	8	13062
Sirius	2014-03-31	ica103010	48	8	13468
Sirius	2014-03-31	ica103020	96	8	13468
Sirius	2014-03-31	ica103030	24	4	13468
Sirius	2014-03-31	ica103040	96	8	13468

^aNumber of individual frames used to create the listed drizzle-combined images.

^bH.E.B. was Principal Investigator for all of these programs.

Table 6. Adjustments to Measures Compiled by Strand and WDS

Date	Sep.	PA ^a	Observer/ Ref. Code ^b	Catalog	Action	Date	Sep.	PA ^a	Ref. Code ^b
	[$''$]	[$^{\circ}$]					[$''$]	[$^{\circ}$]	
1897.83	4.82	329.1	Boothroyd	Strand/WDS	Replaced by	1898.129	4.78	327.52	Boo1898
1897.83	4.80	327.9	See1898c	Strand/WDS	Replaced by	1898.189	4.57	327.12	See1898e
1898.21	4.82	325.3	A_1899b	Strand/WDS	Replaced by	1898.050	4.75	325.12	A_1914d
1898.76	4.97	330.9	A_1899b	WDS	Replaced by	1898.880	4.97	331.11	A_1914d
1899.25	4.99	329.6	A_1900d	WDS	Replaced by	1898.880	4.97	331.11	A_1914d
1902.72	5.33	351.1	Aitken	Strand	Replaced by	1902.241	5.34	345.00	A_1914d
						1902.960	5.33	354.09	A_1914d
1905.14	5.14	6.7	Aitken	Strand	Replaced by	1905.570	5.14	8.68	A_1914d
1910.10	5.21	24.8	Barnard	Strand	Replaced by	1910.025	5.21	26.71	Bar1912
1928.98	2.68	237.9	van den Bos	Strand	Replaced by	1928.824	2.07	231.06	B_1929a
						1929.041	2.14	242.56	B_1929a
						1929.079	3.82	240.06	B_1929a

^aPosition angles are given for J2000 equinox.

^bThe reference code as defined in the Washington Double Star Catalog, <http://ad.usno.navy.mil/wds/Webtextfiles/wdsnewref.txt>. All of the “replaced by” values are taken from the WDS catalog.

Table 7. Ground-Based Measurements of Procyon Used in Orbit Fit

Besselian Date	Sep. [$''$]	J2000 Position Angle [$^{\circ}$]	Ref. Code ^a	Method ^b
1896.930	4.63	320.92	Shb1897a	Ma
1897.000	4.83	321.62	A__1914d	Ma
1897.160	4.65	320.32	Hu_1898	Ma
1897.821	4.66	324.92	Shb1897b	Ma
1898.050	4.75	325.12	A__1914d	Ma
1898.129	4.78	327.52	Boo1898	Ma
1898.189	4.57	327.12	See1898e	Ma
1898.213	4.83	326.52	Bar1898a	Ma
1898.240 ^c	4.26	326.50	Lewis	Ma
1898.282	4.50	325.52	Hu_1903b	Ma
1898.880	4.97	331.11	A__1914d	Ma
1899.073	4.91	331.11	Bar1899	Ma
1899.960	4.88	335.01	A__1914d	Ma
1900.055	5.09	336.54	Bar1900c	Ma
1900.236	4.83	338.81	L__1900	Ma
1900.252 ^c	4.51	327.71	See1911	Ma
1900.295	4.60	332.91	See1900d	Ma
1901.200	5.13	339.00	A__1901b	Ma
1901.300	5.00	338.40	See1911	Ma
1901.883	5.06	343.99	Bar1903a	Ma
1902.214	5.39	345.40	L__1902a	Ma
1902.241	5.34	345.00	A__1914d	Ma
1902.241	5.11	347.00	Hu_1903b	Ma
1902.253 ^c	5.35	338.90	See1911	Ma

Table 7—Continued

Besselian Date	Sep. [$''$]	J2000 Position Angle [$^{\circ}$]	Ref. Code ^a	Method ^b
1902.960	5.33	354.09	A_1914d	Ma
1903.154	5.16	351.52	Bar1903a	Ma
1904.294	4.93	355.69	Bow1904a	Ma
1904.795	5.36	357.87	Bar1909b	Ma
1905.170 ^c	4.46	5.78	L_1905	Ma
1905.570	5.14	8.68	A_1914d	Ma
1909.162	5.26	22.97	Bar1909b	Ma
1909.298	5.04	22.96	Bow1909	Ma
1910.025	5.21	26.71	Bar1912	Ma
1911.060	4.70	29.10	J_1917c	Ma
1911.069	4.69	29.05	J_1911e	Ma
1913.162	5.09	43.00	Bar1913	Ma
1914.300 ^c	6.14	29.50	Bowyer	Ma
1914.939 ^c	5.25	27.93	J_1917c	Ma
1917.241 ^c	4.12	47.82	J_1917c	Ma
1918.220 ^c	4.63	59.22	J_1918b	Ma
1921.214 ^c	5.61	98.90	StG1962a	Ma
1924.190 ^c	5.45	106.88	Dic1962	Ma
1927.106 ^c	3.06	198.97	B_1929a	Ma
1928.824	2.07	231.06	B_1929a	Ma
1929.041 ^c	2.14	242.56	B_1929a	Ma
1929.060 ^c	3.99	251.96	Fin1934b	Ma
1929.079 ^c	3.82	240.06	B_1929a	Ma
1932.272	3.57	278.54	B_1932b	Ma

Table 7—Continued

Besselian Date	Sep. [$''$]	J2000 Position Angle [$^{\circ}$]	Ref. Code ^a	Method ^b
1932.277	3.96	276.04	Fin1934b	Ma
1957.840	4.554	63.51	vAb1958	Po
1957.853	4.573	64.06	The1975	Po
1962.000 ^c	3.90	113.19	B_1962d	Ma
1986.254	5.10	356.27	Wor1989	Ma
1992.720 ^c	5.25	36.30	WGA1994	AO
1995.090	5.12	41.00	Grr2000	CCD

^aThe reference code as defined in the Washington Double Star Catalog, <http://ad.usno.navy.mil/wds/Webtextfiles/wdsnewref.txt>

^bWDS method codes are: Ma (micrometer), Po (photography), CCD (CCD imaging), AO (adaptive optics).

^cObservation rejected from our orbital solution.

Table 8. Elements of Relative Visual Orbit of Procyon

Element	Value
Orbital period, P [yr]	40.840 ± 0.022
Semimajor axis, a [arcsec]	4.3075 ± 0.0016
Inclination, i [deg]	31.408 ± 0.050
Position angle of node, Ω [deg]	100.683 ± 0.095
Date of periastron passage, T_0 [yr]	1968.076 ± 0.023
Eccentricity, e	0.39785 ± 0.00025
Longitude of periastron, ω [deg]	89.23 ± 0.11

Table 9. Parallax and Semimajor Axis for Procyon A

Source	Value	Reference
Absolute Parallax, π [arcsec]		
USNO plates	0.2832 ± 0.0015	Girard et al. (2000)
<i>Hipparcos</i>	0.2846 ± 0.0013	van Leeuwen (2007)
MAP	<u>0.2860 ± 0.0010</u>	Gatewood & Han (2006)
Weighted mean	0.2850 ± 0.0007	
Semimajor Axis, a_A [arcsec]		
~ 600 exposures	1.232 ± 0.008	Girard et al. (2000)

Table 10. Dynamical Masses for Procyon System

Mass	Value
Total mass, $M_A + M_B$	$2.070 \pm 0.016 M_\odot$
M_A	$1.478 \pm 0.012 M_\odot$
M_B	$0.592 \pm 0.006 M_\odot$

Table 11. Error Budgets for Procyon System Dynamical Masses

Quantity	Value	Uncertainty	$\sigma(M_A) [M_\odot]$	$\sigma(M_B) [M_\odot]$
Absolute Parallax, π	0.2850	± 0.0007 arcsec	0.0109	0.0044
Semimajor axis, a	4.3075	± 0.0016 arcsec	0.0019	0.0004
Semimajor axis for A, a_A	1.232	± 0.008 arcsec	0.0038	0.0038
Period, P	40.840	± 0.022 yr	0.0016	0.0006
Combined mass uncertainty			0.012	0.006